Experimental and numerical investigation on the deformation behaviors of large diameter steel tubes under concentrated lateral impact loads

Yongli Ren , Zhaolong Yu , Xugang Hua , Jørgen Amdahl , Zili Zhang , Zhengqing Chen

PII: S0734-743X(23)00207-5
DOI: https://doi.org/10.1016/j.ijimpeng.2023.104696
Reference: IE 104696

To appear in: *International Journal of Impact Engineering*

Received date: 3 March 2023
Revised date: 13 May 2023
Accepted date: 7 June 2023

Please cite this article as: Yongli Ren , Zhaolong Yu , Xugang Hua , Jørgen Amdahl , Zili Zhang , Zhengqing Chen , Experimental and numerical investigation on the deformation behaviors of large diameter steel tubes under concentrated lateral impact loads, *International Journal of Impact Engineering* (2023), doi: https://doi.org/10.1016/j.ijimpeng.2023.104696

Highlights

- Deformation behaviors of large diameter steel tubes from a floating offshore wind tube (FOWT) against impact loads were investigated by experiments and numerical simulations.
- Global motions of the tubes in the experiments were accounted for by a single-degree-of-freedom model for the rigid body motions of the FOWT.
- Impact force-deformation curves, tube deformation patterns and energy dissipation were compared and discussed.
- A nondimensional force-deformation curve was recommended for the design of large diameter steel tubes under impact loads.

Experimental and numerical investigation on the deformation behaviors of large diameter steel tubes under concentrated lateral impact loads

Yongli Ren[a], Zhaolong Yu[b,c], Xugang Hua[a], Jørgen Amdahl[b,c], Zili Zhang[d], Zhengqing Chen[a]

[a]Key Laboratory for Bridge and Wind Engineering of Hunan Province, College of Civil Engineering, Hunan University, Changsha, Hunan, China

[b]Department of Marine Technology, Norwegian University of Science and Technology, Norway

[c]Centre for Autonomous Marine Operations and Systems, Norwegian University of Science and Technology, Norway

[d]School of Civil Engineering, Tongji University, Shanghai, China

Abstract

Large diameter steel tubes are widely used in bottom fixed and floating offshore wind turbines. Offshore wind turbines (OWTs) operating in the oceans are exposed to the risk of collisions when ships pass and dock at turbines. Thus, it is extremely important to investigate the impact mechanics of ship-OWT collisions and propose practical designs for methods to protect OWTs from collision loads. This paper presents a series of experimental and numerical studies on the deformation behaviors of large diameter steel tubes from a NREL 5 MW spar-type floating offshore wind turbine (FOWT) under lateral impact loads. These studies consider the effects of different impact velocities, attached masses, diameters and thicknesses of the tubes on their response to impact loading. In these experiments, a rigid indenter was mounted on a pendulum system and accelerated to strike the tubes; the scale was 1:30. The dimensions of the indenter head were much smaller than the tube diameter in order to concentrate the impact load. Global motions of the impacted tubes

were modeled by springs introduced at the boundaries, and their stiffnesses were determined according to an equivalent single-degree-of-freedom (SDOF) model. Numerical simulations of the experiments were conducted using the nonlinear finite element (FE) software LS-DYNA. The experimental and numerical results were compared and discussed with respect to force-deformation curves, deformation modes and energy dissipation. Existing theoretical solutions for the lateral indentation resistance of tubes were also compared to the experimental and numerical simulation data. The results indicated needs for new solutions when the impact loads become concentrated.

Keywords

floating offshore wind turbine; ship collision; steel tube; impact experiment; concentrated loads; deformation

1. Introduction

Offshore wind energy is a clean renewable energy that is becoming increasingly competitive in the energy market. Offshore wind turbines (OWTs) can generally be classified into two categories: bottom fixed OWTs and floating offshore wind turbines (FOWTs). Bottom fixed OWTs are mounted on foundations like monopiles, tripods and jackets that rest on seabed. They are very cost effective and are suitable for shallow waters (< 50 m). FOWTs become attractive for deep waters and they are often mounted on floaters of different types such as the spar-type, the semisubmersible-type, the tension leg-type, and the barge-type [1]. OWTs are often located near coastal areas with traffic lanes where they are exposed to the risk of collisions with ships that dock to provide construction, operation and maintenance as well as passing commercial ships. It is therefore crucial to assess the dynamic responses and structural damages of OWTs subjected to ship collisions and to design structures against such accidental loads [2].

Nonlinear finite element analysis (NLFEA) is often used to investigate the structural responses of OWTs in ship collisions. For ship collision with bottom fixed OWTs, Moulas et al. [3] used ABAQUS to study 4000 tons class vessels colliding with a monopile OWT and a jacket OWT. The results showed that collision energy, contact area and vessels heights influenced the turbine damage extent. Bela et al. [4] and Song et al. [5] investigated the responses of a monopile OWT collided by rigid and deformable ship bows. With a rigid ship, significant plastic deformations of the OWT were observed in the impacted region and near the mudline, and collapse of the entire structure occurred when the impact velocity exceeded 5 m/s. While with a deformable ship, the turbine local deformations were much smaller than those caused by a rigid ship. The effects of aerodynamic damping, ship impact velocities, mean wind speeds, wind directions, and ship bow stiffnesses on the turbine global responses and local damage were discussed by Song et al. [5]. Lee [6] studied the dynamic response and damage of a tripod OWT collided by a barge and compared the damage with that of the wind turbine installed with a protective device made of rubber.

For ship collision with FOWTs, Echeverry et al. [7] and Ren et al. [8] studied global responses and local damages of the NREL 5MW spar-type FOWT [9, 10] subjected to ship collisions using LS-DYNA, where the hydrodynamic effects were considered by MCOL [11]. The effects of rigid and deformable ship bow and impact velocity were analyzed. Zhang et al. [12] and Zhang and Hu [13] also investigated ship collision responses of the NREL 5MW spar-type FOWT considering the aero-hydro-structure coupling effects using an in-house code and the user-defined load subroutine in LS-DYNA. The results showed that the turbine tower collapsed at a high-speed impact of 5 m/s and it became more critical under combined wind and wave loads. Yu et al. [2] investigated the dynamic responses of a 10 MW semi-submersible FOWT mounted on an

OO-STAR floater under collisions from ships of 7500 and 150000 tons in terms of parked and operative conditions using NLFEA. The results showed that the combined actions of collision loads, wind thrust and tightened mooring lines may significantly amplify the pitch motion of the floater and lead to possible capsizing. A detailed review of recent developments related to ship-OWT collisions can be found in Ladeira et al. [14].

Steel tubes with circular section tubes are important structural members that are widely used in OWTs and other civil and offshore structures because of their architectural and mechanical advantages. Extensive studies of steel tubes under lateral loads have been conducted using experiments, numerical simulations and analytical methods, and the results can be found in the literature. Experiments on thin-walled tubes with circular cross sections under mid-span transverse loading were reported in Refs. [15-17], and the deformation modes were identified for the tubes with simply supported boundary conditions. Soares and Søreide [18] conducted a plastic analysis of laterally loaded circular tubes with various boundary conditions and a rigid perfectly plastic material. Jones [19] examined the accuracy of quasi-static methods for predicting the inelastic behavior in structures and found good agreement with experimental results. Ong and Lu [20] conducted quasi-static tests to study the collapse loads and energy-absorbing capabilities of mild steel tubes. Jones and Shen [21] and Zhu et al. [22] investigated the failure mechanism of a fully clamped pipeline impacted by a rigid wedge-shaped indenter at different impact positions. Based on the experimental observations and results, a theoretical model based the rigid-plastic method was developed to predict the impact response of pipes [21]. Zhang et al. [23] studied the plastic behavior of steel tubes subjected to transverse low-velocity mass impact and lateral quasi-static loading. Four deflection modes and four failure modes were identified respectively.

Zhi et al. [24] utilized experiments to study axially preloaded circular tubes subjected to transverse impacts and found that axial tension enhanced greatly the load carrying capability by membrane effects, while the capacity reduced significantly under axial compression. Søreide and Amdahl [25] studied experimentally the impact resistance and deformation modes of both axially free and constrained tubular members and demonstrated increased energy absorption capabilities by developing membrane forces. For the indentation resistance of tubes, Amdahl [26] proposed a semi-analytical model based on the plastic yield line analysis considering a flat indenter of varied widths. The model was adopted in NORSOK N-004 [27] for design against ship collisions. Wierzbicki and Suh [28] derived a closed form analytical solution for large indentation resistance of tubes subjected to combined loading of lateral impact loads, bending moments and axial force at the boundaries. Yu and Amdahl [29] conducted a comprehensive review of research studies on collisions of ships with offshore tubular structures, that covers broad aspects of the impact responses of tubular structures and assessment procedures.

From the literature review, extensive research works have been carried out on the impact responses of tubes. These studies, however, generally focused on long slender tubes, where the impacting indenter was much wider than the tube diameter. For OWT applications with large diameter tubes, ship collision loads become more concentrated. It remains unclear whether existing analytical models apply to such scenarios. This is especially relevant when ships with bulbous bows collide with OWTs.

This paper conducted a series of scaled experiments to study the deformation behaviors of large diameter steel tubes from a NREL 5 MW spar-type FOWT under ship bulbous bow collisions. The scaled indenter has a much smaller width compared to the tube diameter, which yields

concentrated impact loading. Global motions of the impacted tubes were scaled using an equivalent single-degree-of-freedom (SDOF) model as described in Section 2. This is followed by detailed descriptions of experimental setups and test scenarios in Section 3 and finite element (FE) modelling in Section 4. The experimental and numerical results are compared and discussed with respect to force-deformation curves, deformation modes and energy in Section 5.

2. A SDOF model for rigid body motions of FOWT subjected to collision loads

In this study, the well-documented NREL 5 MW spar-type FOWT [9, 10] was selected for ship collision analysis and its main dimensions are described in Table 1.

Table 1 Parameters of the 5 MW spar-type floating offshore wind turbine [9, 10]

Parameter	Value
Tower height, $\boldsymbol{h_T}$	77.6 m
Spar height above taper top, $\boldsymbol{h_{S1}}$	14 m
Spar taper height, $\boldsymbol{h_{S2}}$	8 m
Spar height below taper bottom, $\boldsymbol{h_{S3}}$	108 m
Spar draft, $\boldsymbol{h_S}$	130 m
Diameter of spar above taper, $\boldsymbol{D_1}$	6.5 m
Diameter of spar below taper, $\boldsymbol{D_2}$	9.4 m
FOWT's COG below SWL, $\boldsymbol{h_G}$	78 m
FOWT's COB below SWL, $\boldsymbol{h_B}$	62 m
FOWT's mass, $\boldsymbol{M_{r11}}$	8.066×10^6 kg
FOWT's inertia about COG in pitch, $\boldsymbol{M_{r22}}$	1.895×10^{10} kg·m^2
Height from spar bottom to SWL	120 m
Unstretched Mooring line length	902.2 m
Fairlead depth below SWL	70 m
Water depth	320 m

2.1. Equation of motions for a spar-type FOWT

By neglecting the influence of structural flexibilities, the rigid body motions of the NREL 5 MW spar-type FOWT were simplified as a 2-DOF model as shown in Fig. 1 including the surge motion, q_1, and the pitch motion, q_2, respectively. This model was described in a body fixed coordinate $OX_1X_2X_3$ with its origin at the center of gravity (COG) of the undeformed system. According to the results of Refs. [8], [30] and [31], the equation of motion for the 2-DOF model is as follows:

$$(\boldsymbol{M}_r+\boldsymbol{M}_a)\ddot{\boldsymbol{X}} + (\boldsymbol{G} + \boldsymbol{C}_{aero} + \boldsymbol{C}_{rad} + \boldsymbol{C}_{vis})\dot{\boldsymbol{X}} + \left(\boldsymbol{K}_{buoy} + K_{moor}\right)\boldsymbol{X} = \boldsymbol{F}_C(t) \quad (1)$$

where $\boldsymbol{M}_r$ is the structural mass matrix, $\boldsymbol{M}_a$ is the hydrodynamic added mass matrix, $\boldsymbol{G}$ is the gyroscopic matrix, $\boldsymbol{C}_{aero}$ is the aerodynamic damping matrix, $\boldsymbol{C}_{rad}$ is the wave-making radiation damping matrix, $\boldsymbol{C}_{vis}$ is the viscous damping matrix, $\boldsymbol{K}_{buoy}$ is the hydrodynamic restoring matrix, $\boldsymbol{K}_{moor}$ is the linear stiffness matrix of the mooring system, and $\boldsymbol{X} = [q_1,q_2]^{\mathrm{T}}$ is the 2-DOF displacement vector in surge and pitch, respectively. $\boldsymbol{F}_C$ is the contact force vector.

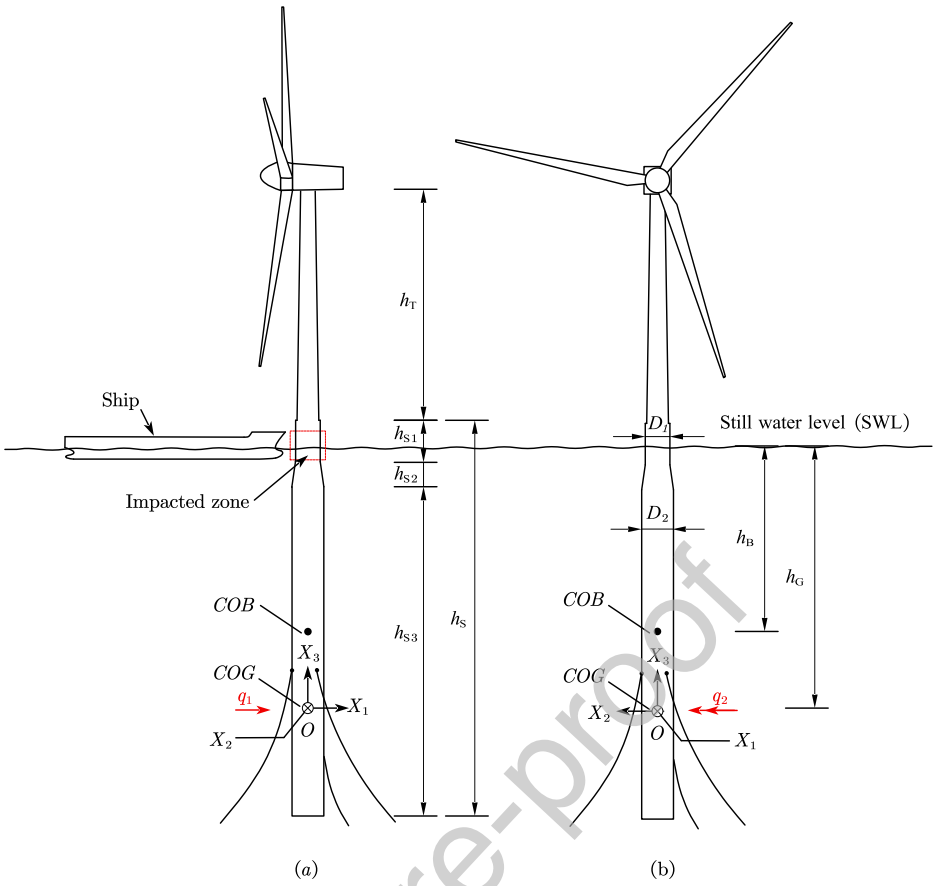

Fig. 1. 2-DOF rigid model of the spar-type FOWT.

The experiment was intended to investigate the local deformation of the spar-type FOWT considering the motions of the wind turbine in the impacted region, as shown in Fig. 2 (a). To fulfill this objective, the 2-DOF rigid body motion model was rescaled into an equivalent SDOF model with an equivalent mass, damping and stiffness, as shown in Fig. 2 (b) and (c).

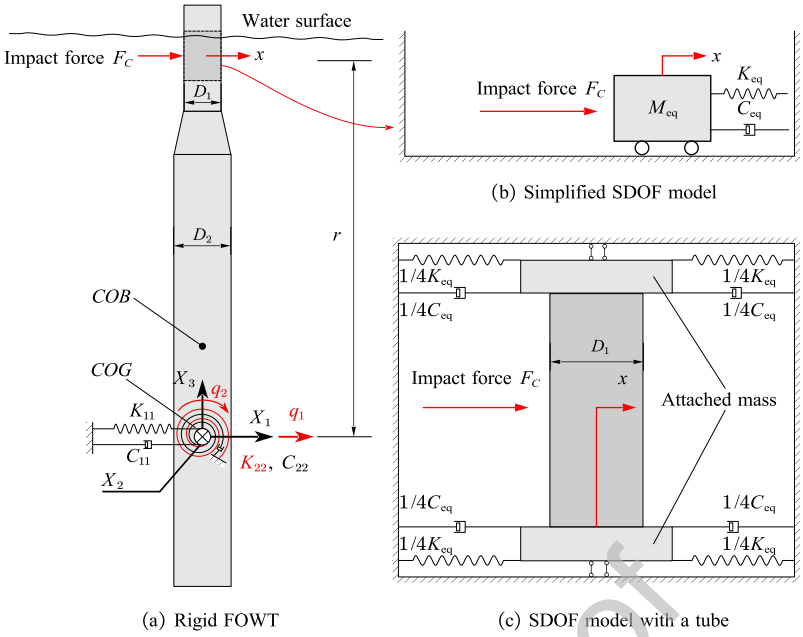

Fig. 2. Equivalent SDOF model with a steel tube.

(1) Equivalent mass

Ship collision loads are characterized by large force amplitudes and short durations (in seconds) compared to the natural periods of the rigid body motion of the platforms. Within a short collision period, the velocities and displacements of a FOWT are relatively small, but accelerations can be large. This indicates that the collision force (instantaneous load) is mainly resisted by inertia forces, and the damping and stiffnesses forces from hydrodynamics, hydrostatics and mooring lines are considered secondary. Therefore, the equation of motion of the 2-DOF rigid model in Eq. (1) can be simplified as follows:

$$\begin{bmatrix} M_{11} & M_{12} \\ M_{21} & M_{22} \end{bmatrix} \begin{Bmatrix} \ddot{q}_1 \\ \ddot{q}_1 \end{Bmatrix} = \begin{Bmatrix} F_C \\ F_C r \end{Bmatrix} \qquad (2)$$

where $M_{11} = M_{r11} + M_{a11}$, $M_{12} = M_{21} = M_{a12} = M_{a21}$ and $M_{22} = M_{r22} + M_{a22}$. r is the distance from the impacted point to the COG. The values of these parameters are given in Table 2 for the NREL 5 MW spar-type FOWT.

Table 2. Parameters in Eqs. (3) and (5) [9, 10].

Parameter	Value
$\boldsymbol{M_{a11}}$	8.160×10^{6} kg
$\boldsymbol{M_{a12}}$	1.398×10^{8} kg·m
$\boldsymbol{M_{a22}}$	1.095×10^{10} kg·m^2
$\boldsymbol{K_{11}}$	4.118×10^{4} N/m
$\boldsymbol{K_{22}}$	1.285×10^{9} N·m
r	74 m

The corresponding equivalent SDOF model is shown in Fig. 2 (b), where the equivalent motion equation without considering the damping and stiffness becomes $M_{eq}\ddot{x} = F_C$ and the geometric relationship yields $\ddot{x} = \ddot{q}_1 + \ddot{q}_2 r$. Combining Eq. (2), the equivalent mass M_{eq} can be written as:

$$M_{eq} = \frac{M_{11}\alpha + M_{12}}{\alpha + r} \tag{3}$$

where $\alpha = \frac{M_{22} - rM_{12}}{rM_{11} - M_{21}}$.

(2) Equivalent static stiffness

By neglecting the inertia and damping terms, the problem becomes a simple static equilibrium problem, where the stiffness forces induced by displacements of q_1 and q_5 in surge and pitch shall balance the external force *F*, then Eq. (1) becomes:

$$\begin{bmatrix} K_{11} & 0 \\ 0 & K_{22} \end{bmatrix} \begin{Bmatrix} q_1 \\ q_5 \end{Bmatrix} = \begin{Bmatrix} F \\ Fr \end{Bmatrix} \tag{4}$$

where K_{11} and K_{22} are the stiffness of the FOWT in surge (mooring stiffness) and pitch (hydrostatic stiffness). The values of K_{11} and K_{22} are given in Table 2.

The equivalent stiffness in the SDOF model can be expressed as $K_{eq} = F/x_{eq}$, where $x_{eq} = x_1 + \varphi r$ is the equivalent displacement. The equivalent stiffness can then be expressed as:

$$K_{eq} = \frac{K_{11}K_{22}}{K_{11}r^2+K_{22}} \quad (5)$$

(3) Damping

Generally, for a floating offshore structure, the damping C_{eq} from hydrodynamics could be 5 ~ 10% of the critical damping C_{cr} [32], thus:

$$C_{eq} = 0.05\sim0.1C_{cr} \quad (6)$$

where $C_{cr} = 2\sqrt{K_{eq}M_{eq}}$.

The natural period of the SDOF model can be calculated using the definition of $T_{eq} = 2\pi\sqrt{\frac{M_{eq}}{K_{eq}}}$, which yields a value of 73 s. This period is shorter than the period of the spar-type FOWT in surge (125 s), but longer than the period in pitch (30 s). The equivalent mass of the SDOF model is 4.735×10^6 kg, which accounts for only 29% of the FOWT's total mass, including the hydrodynamic added mass due to coupled motion effects.

2.2. Verification of the SDOF model

To verify the SDOF model, an artificial impact load history in Fig. 3 (a) was applied at the impact point on the rigid FOWT to obtain dynamic responses and enable a comparison. The accelerations and displacements for the two models were in good agreement during and after impact, as shown in Fig. 3 (b) and (c). The variation in damping (damping ratio $\zeta = \frac{C_{eq}}{C_{cr}} \times 100\%$) within a normal range has little influence on the responses. Therefore, the proposed SDOF model captured global motions of the impact point on the rigid FOWT very well and can be used to design model tests.

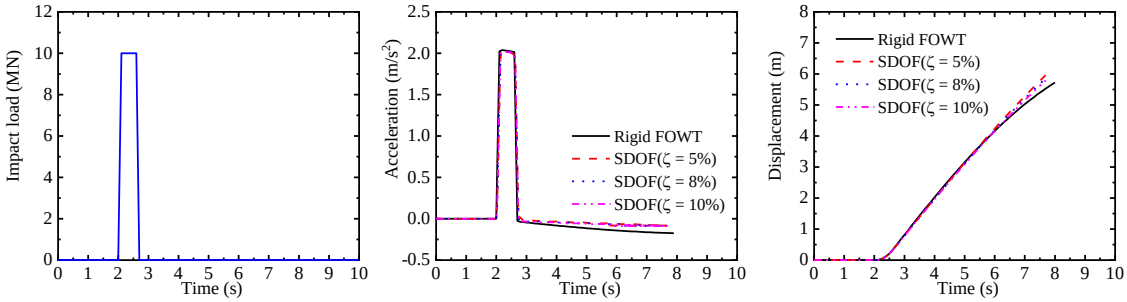

(a) Impact load (b) Acceleration (c) Displacement

Fig. 3. Comparison of the responses of the rigid FOWT and SDOF models at the impact region.

3. Experimental setup

3.1. Experimental equipment and test instruments

To examine the deformation behaviors of large diameter steel tubes from a spar-type FOWT subjected to lateral impact loads, new experimental equipment was designed, as shown in Fig. 4 and Fig. 5, which included braced frames, a sliding component, boundary springs, a cylindrical indenter mounted on a single pendulum, and air cylinders. The sliding component consisted of guide rails, sliders and two end plates with attached mass blocks. Test specimens of the scaled steel tubes with welded flanges (240 mm×240 mm×6 mm) at the two ends were connected to the sliding component by bolts such that they could slide along the guide rails during and after impact. The mass and the boundary spring stiffnesses could be adjusted according to the SDOF model. The damping in the experimental SDOF system originated from friction between the sliders and the guide rails. The mass and the maximum velocity of the single pendulum were 101 kg and 3m/s, respectively. The single pendulum was released by air cylinder 1 to obtain the kinetic energy and then pulled back by air cylinder 2 after the first collision with the steel tubes to avoid a second collision. Both the diameter and length of the indenter mounted on the single pendulum were 50 mm.

To measure various parameters, several instruments were used in the experiments. An

accelerometer was mounted on a slider to measure the acceleration of the sliding component, as shown in Fig. 5 (a), while another accelerometer was mounted on the pendulum to measure its acceleration, as shown in Fig. 5 (c). A piezoelectric force transducer (load cell) to measure the impact force was installed between the indenter and the pendulum, as shown in Fig. 5 (c). To monitor the strain, eight strain gauges were attached onto the outer surface of the steel tubes, as shown in Fig. 5 (a) and (b). A high-speed video camera was used to measure the motions of the sliding component and the single pendulum at a speed of 1600 frames per second. Also, a laser displacement meter was installed inside the tube to measure the permanent deformation with an auxiliary approach, as shown in Fig. 4 (c).

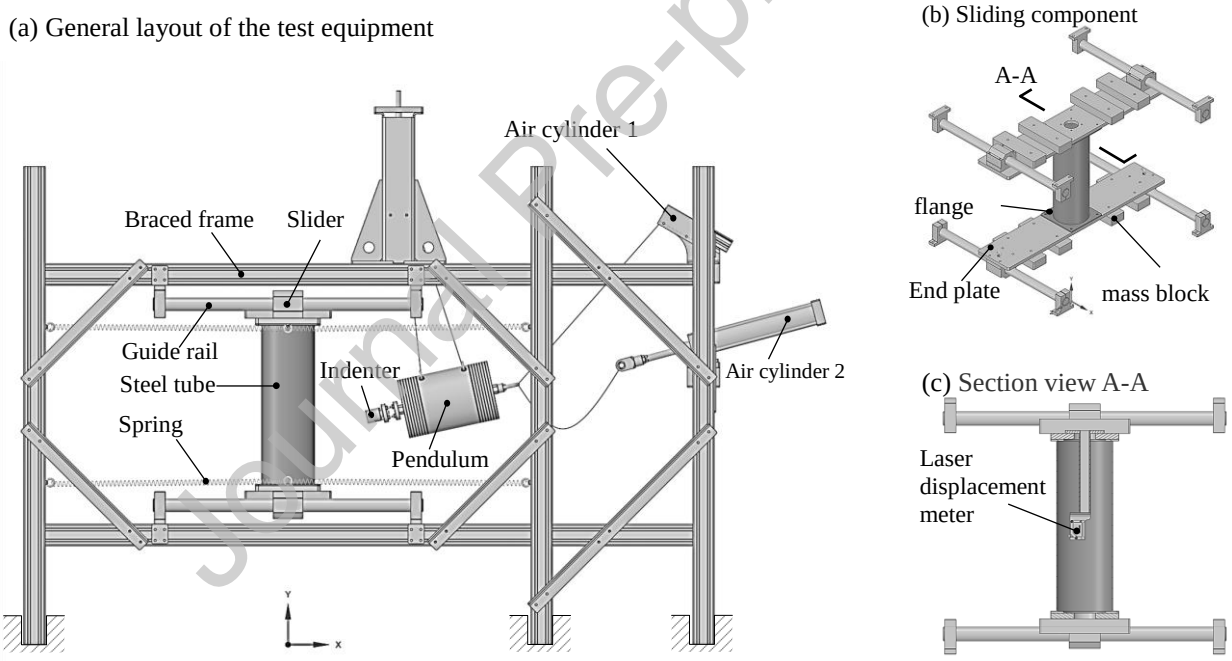

Fig. 4. Schematic diagram of the test equipment

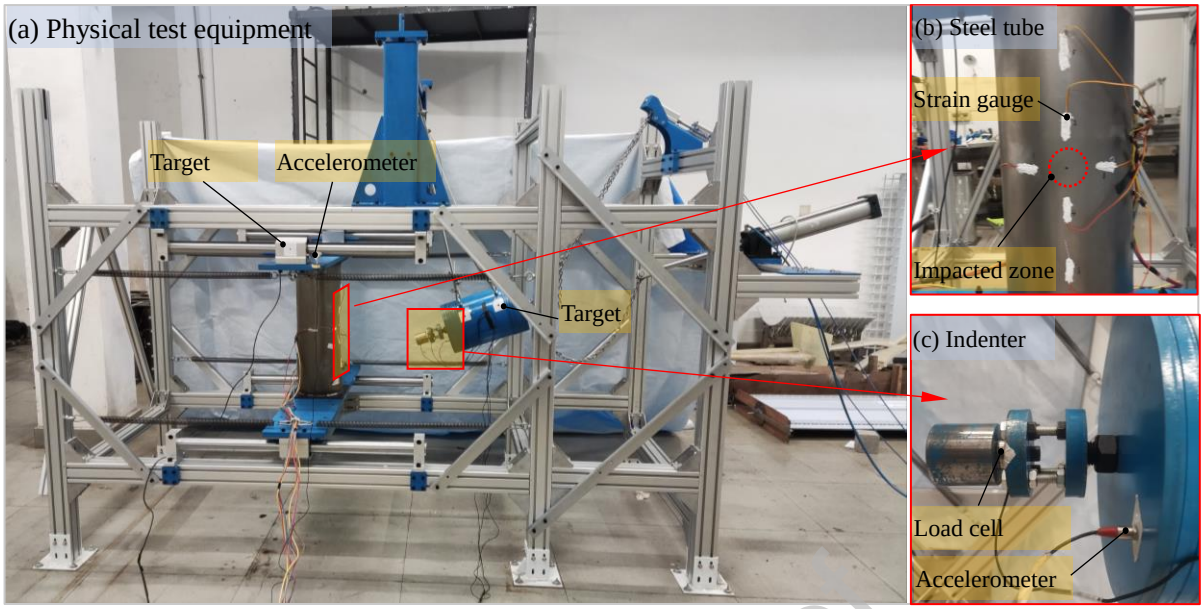

Fig. 5. Physical test equipment and instruments.

3.2. Experiment design and manufacture

A geometric scale of $\lambda = 1:30$ was adopted in the present work, and other scale factors of different physical quantities are summarized in Table 3. In the prototype of FOWT, the impact point is usually close to the SWL, and a taper in the spar is 4 m below the SWL. In a preliminary study, a steel tube with a diameter of 6.5 m, length of 18 m and thickness of 40 mm was scaled for the impact tests, with the impact point 4 m below the SWL, namely, r =74 m. The FOWT's mass and stiffnesses were first converted to the mass and stiffness of the SDOF model mass and stiffness, which was then scaled for test purposes. The detailed values of the prototype and model can be found in Table 4, and some values for the model were reasonably adjusted according to the experimental feasibility. The spring stiffness in the SDOF system is 35032 N/m in full scale and is 1167 N/m after scaling. The scaled spring stiffness is found to be too small such that during the test, the sliders will collide into constraint components at the ends of the guide rails. In order to avoid such collisions, an increase of the spring stiffness to 1960 N/m was adopted. This, however, is believed to have negligible effects on the tube damage and impact resistance. Generally, the actual

ship collision process takes around 2 seconds in full scale, while the studied platform has a natural period of 73 seconds, resulting in a ratio of approximately 0.027. The tube barely moves within the short impact period. Therefore, the spring stiffness variation does not influence much the tube damage and impact resistance [33].

Table 3. Main scale factors of the test model.

Physical quantity	Dimension	Scale factor
Length	[L]	λ
Mass	$[FL^{-1}T^2]$	λ^3
Force	[F]	λ^2
Acceleration	$[LT^{-2}]$	$\frac{1}{\lambda}$
Time	[T]	λ
Velocity	$[LT^{-1}]$	1
Energy	[FL]	λ^3

Table 4. Prototype and model values.

Parameter	Value	
	Prototype	Model
SDOF model Mass, M_{eq}	4.74×10^6 kg	175.4 kg (182.6 kg)
Spring stiffness, K_{eq}	35032 N/m	1167 N/m (1960 N/m)
Tube length	18 m	600 mm
Tube diameter	6.5 m	210 mm (200 mm)
Tube thickness	40 mm	1.33 mm (1.2 mm)
Note: The values in brackets were used in the experiments.		

Fourteen specimens of steel tubes were manufactured and divided into 4 groups to study the

effects of different impact velocities, attached masses, diameters and thicknesses on the damage of the steel tubes. The steel tubes in the experiment were made of Q345 steel (yield stress 345 MPa). The steel tubes were manufactured fully in-house by cold rolling of flat plates and then welding. The impact scenarios are summarized in Table 5.

Table 5. Steel tube specimen design.

Cases	Total mass (kg)	Steel tube mass (kg)	Attached mass (kg)	Impact velocity (m/s)	Diameter (mm)	Wall thickness (mm)
CS01	182.6	3.5	179.1	**0.89**	200	1.2
CS02	182.6	3.5	179.1	**1.29**	200	1.2
CS03	182.6	3.5	179.1	**1.85**	200	1.2
CS04	182.6	3.5	179.1	**2.35**	200	1.2
CS05	182.6	3.5	179.1	**2.79**	200	1.2
CS06	**110.6**	3.5	107.1	1.85	200	1.2
CS07	**146.6**	3.5	143.1	1.85	200	1.2
CS08	**218.6**	3.5	215.1	1.85	200	1.2
CS09	**254.6**	3.5	251.1	1.85	200	1.2
CS10	182.2	3.1	179.1	1.85	**180**	1.2
CS11	182.9	3.8	179.1	1.85	**220**	1.2
CS12	183.3	4.2	179.1	1.85	**240**	1.2
CS13	183.4	4.3	179.1	1.85	200	**1.5**
CS14	184.9	5.8	179.1	1.85	200	**2.0**

3.3. Material properties

To obtain the stress-strain curves of the test tubes, four groups of flat dog-bone specimens were prepared according to the test method specified in GB/T 228.1-2010 [34] for uniaxial tensile tests, as shown in Fig. 6 (a). This gives a gauge length of 61.89 mm, 69.20 mm and 79.90 mm for the tensile specimens, with thicknesses of 12 mm, 15 mm and 20 mm, respectively. The tensile

specimens in SP12-1~2 with arcs were cut from the tested tubes. A testing machine in the lab with a capacity of 1000 KN was utilized to perform the tensile tests. Fig. 7 shows the resulting stress-strain relationships from the uniaxial tensile tests, and the fractured specimens are given in Fig. 6 (b), (c), (d), and (e). The results indicate increased stresses in the strain hardening stage due to initial deformations from cold rolling.

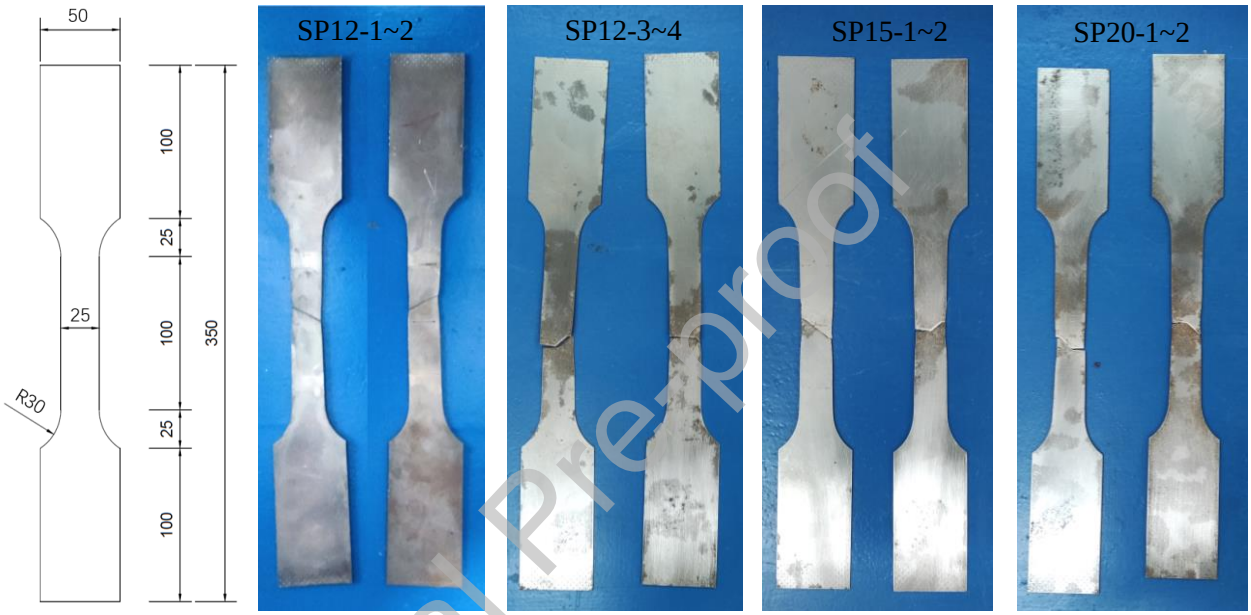

(a) (b) (c) (d) (e)

Fig. 6. Uniaxial tensile test for Q345 steel: (a) dimensions of the tensile specimen; (b) 1.2 mm specimen cut from the tube; (c), (d) and (e) displaying the specimens cut from the same parent plate as the tubes, with a thickness of 1.2 mm, 1.5 mm, 2.0 mm, respectively.

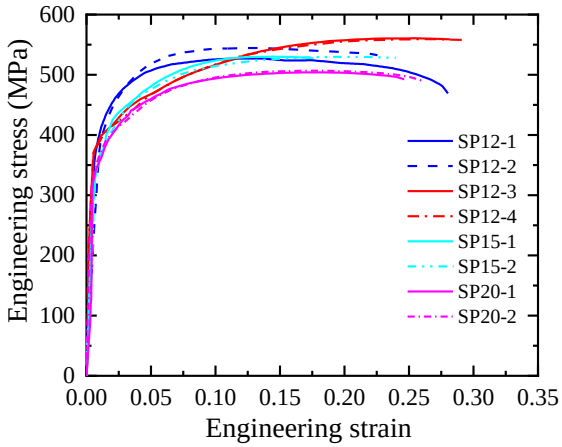

Fig. 7. Engineering stress-strain curve of Q345 steel.

4. Numerical modelling

4.1. FE models

The nonlinear FE code LS-DYNA was used to reproduce the experiments and corresponding FE models were established, as shown in Fig. 8. The 4-node Belytschko-Tsay shell elements with reduced integration were used for the steel tubes [35]. In order to capture the stress and strain field adequately, fine meshes were used for discretizing the steel tubes with a mesh of 2 mm. This gives reasonable ratios of the element length over thickness [36]. The two end plates and the flanges were modeled by the same shell elements and they were connected by sharing common nodes at the bolt holes. Mass elements were attached on the nodes of the end plates to represent the mass blocks in the experiments, as shown in Fig. 8 (b).

The indenter and pendulum were simulated by the 8-node solid elements, and the connecting bolts were simulated by beam elements. The initial kinetic energy of the pendulum in FE models was determined by the impact velocity from the experiments. The master-slave contact was adopted for modelling the contact between the indenter and the struck tube. The self-contact was used for possible contacts due to tube deformation. A friction coefficient of 0.3 was used.

Eight spring and damper elements were used to simulate the system stiffness and damping. The spring and damper elements connected to the end plates at one end and were fully constrained at the other end. The spring stiffnesses match those from the experiments. The system damping was set to 45.3 N·s/m as obtained from the experimental-free-vibration attenuation curve [37]. The four short edges of the end plates were fully constrained in the Y and Z directions and were allowed to move freely in the X direction.

4.2. Material modelling

The piecewise linear plasticity model (MAT_PIECEWISE_LINEAR_PLASTICITY) was used

to simulate the material behaviors of the Q345 steel used in the experiments. The true stress–strain curves calculated from the uniaxial tensible test curves were used as inputs [38]. The Cowper-Symonds constitutive model was adopted to consider the strain rate effects [39]:

$$\frac{\sigma_d}{\sigma_s} = 1 + \left(\frac{\dot{\varepsilon}}{C}\right)^{\frac{1}{p}} \quad (7)$$

where σ_d and σ_s are the true dynamic stress and static stress, respectively. C and p are material constants for the strain rate effects. For the Q345 steel material used in the test, C=4000 and p=5 were adopted following the recommendation in Stroheim and Amdahl [40]. The end plates, flanges, indenter and pendulum were made of Q235 steel with a yield stress of 235 MPa.

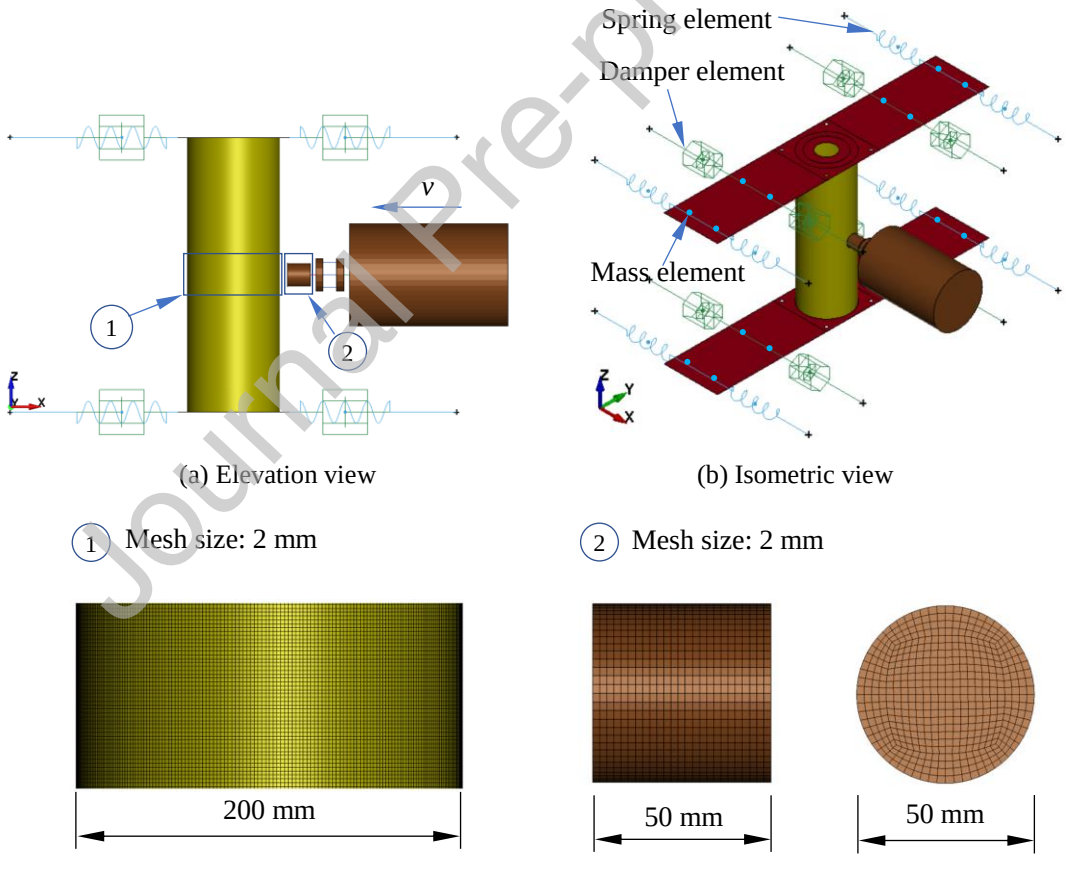

Fig. 8. Finite element models of the steel tube and pendulum.

5. Results and discussions

5.1. Test group 1: CS01~05 with different impact energies

Fig. 9 shows plots of the typical impact force-time history and impact force-deformation curves from the experiment (EXP) and the finite element method (FEM) with impact velocities of 0.89 m/s and 2.79 m/s, respectively. Numerical simulation curves with and without strain rate effects are presented. The experimental and numerical curves show reasonable agreement in the initial stage but tend to deviate after some time and the experiments yielded smaller peak forces than the numerical results. In addition, the impact force-time histories in the tests exhibit multiple peaks instead of one peak. This may be because of the rigid body rotation of the striking indenter close to the maximum deformation, which loosened the supporting ropes, as shown in Fig. 11. Fig. 9 (b) shows that the slopes of the force-deformation curves in the tests agreed with the numerical results without strain rate at a low impact energy, but not well at a high impact energy. However, when the strain rate effects with C=4000 and p=5 were considered, the differences in the slopes decreased at high impact energy. The results in Fig. 10 show that the impact force-deformation curves could be divided into three phases that reveal the deformable process of the tubes: (Ⅰ) initial collapse, where local dents that resemble the shape of the indenter formed on the tubes, and the slopes of force-deformation curves in the tests were steep and agreed well with the numerical modelling results. (Ⅱ) damage extension stage, in which the damage on the tubes continuously extended in the longitudinal and circumferential directions, and the slopes between the tests and numerical models displayed some evident discrepancies if the strain rate effects were ignored. (Ⅲ) unloading, where some elastic recoveries of deformations occurred on the tubes prior to completely separate with the indenter.

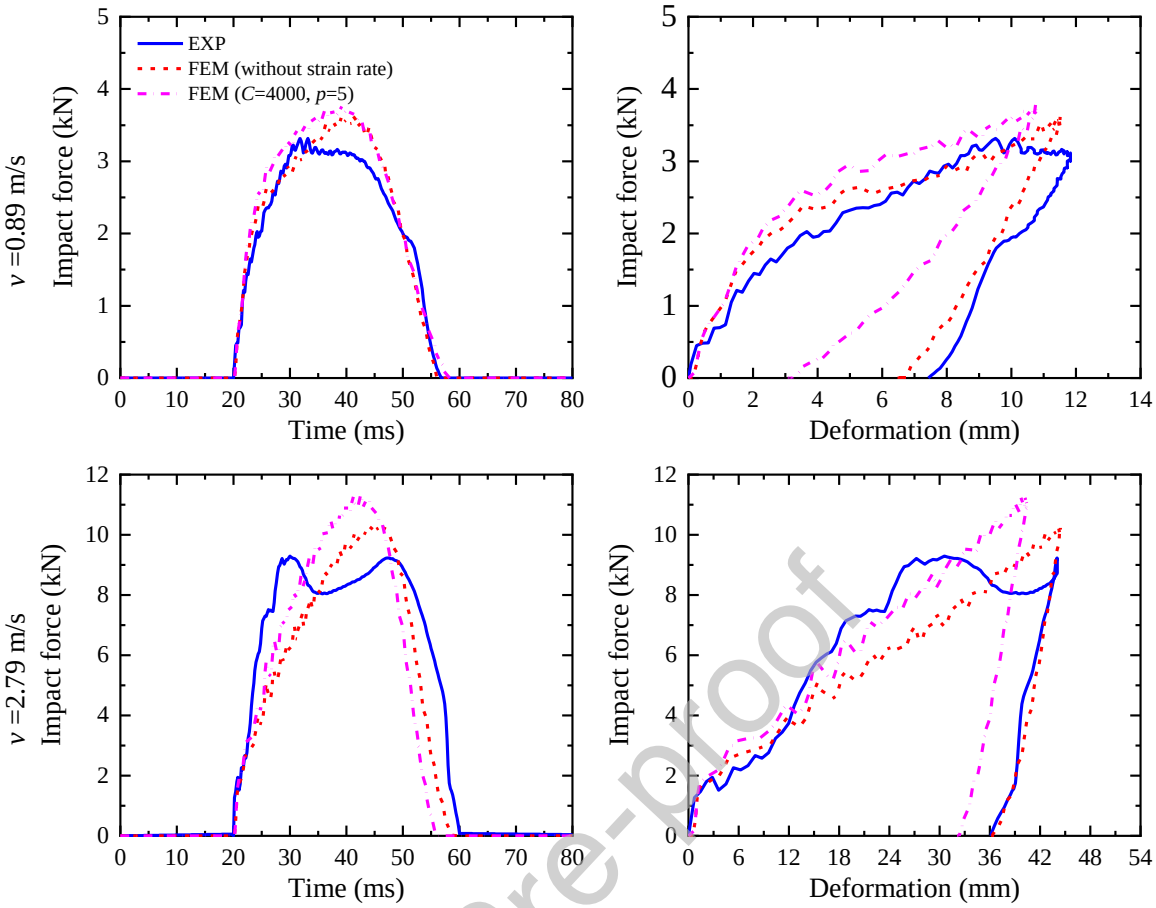

(a) Force versus time (b) Force versus deformation

Fig. 9. Impact force-time history and impact force-deformation curves for different impact velocities.

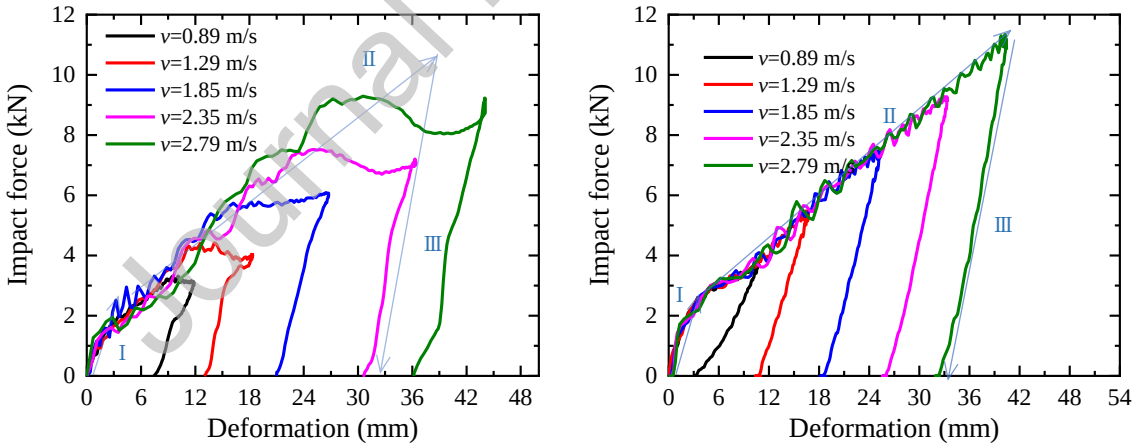

(a) Experiment (b) FEM (*C*=4000, *p*=5)

Fig. 10. Force versus deformation curves for different impact velocities.

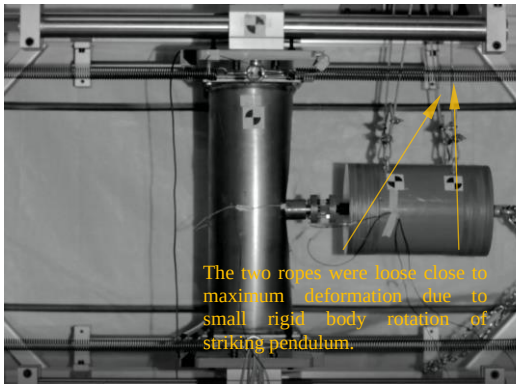

Fig. 11. A frame captured by the high-speed camera during impact.

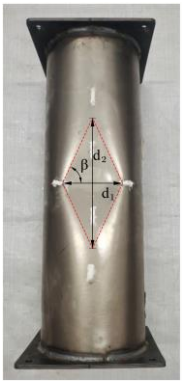

Fig. 12. Schematic diagram of measurement of the shape of the local damage on the tube.

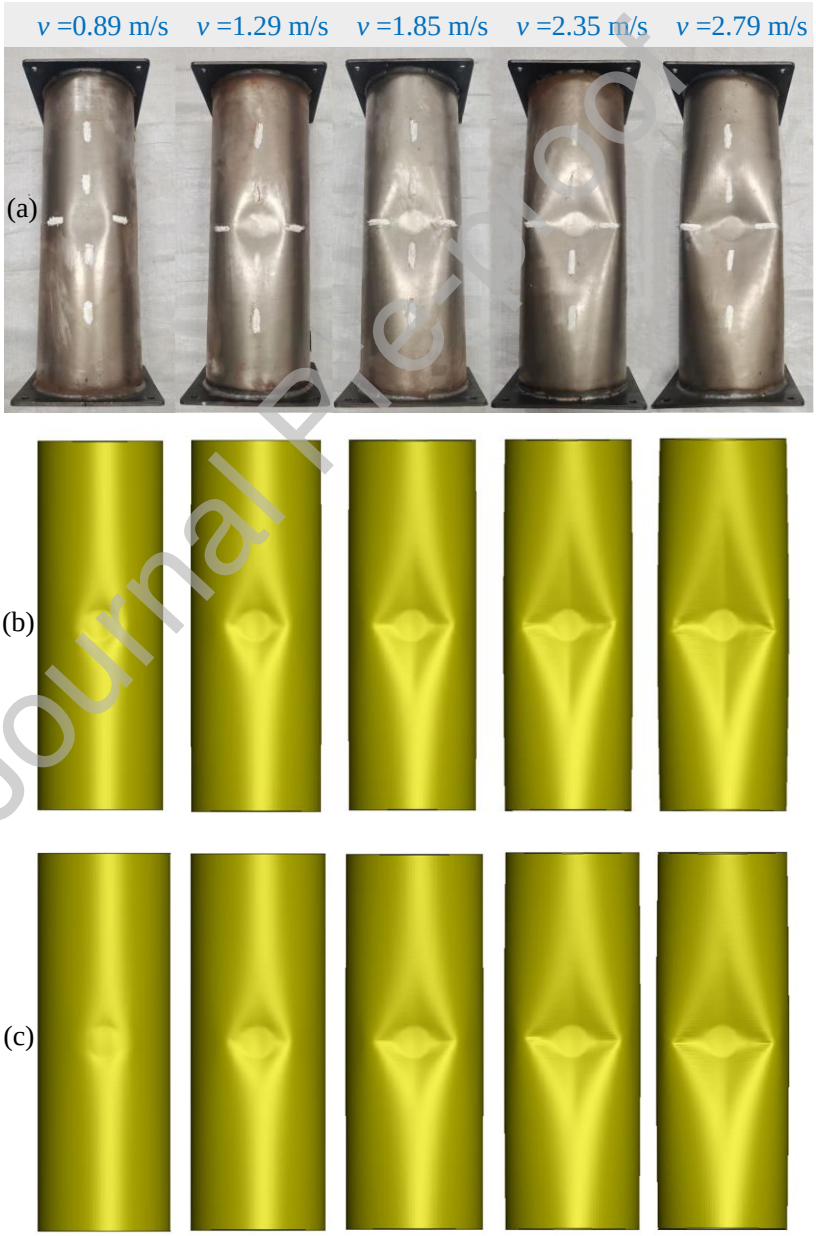

Fig. 13. Deformation modes of steel tubes under different impact velocities: (a) experiment, (b) FEM (without

strain rate) and (c) FEM (C=4000 and p=5).

Fig. 13 (a) shows the tube damage for the corresponding cases of CS01~05. Results show that the tube deformation modes were governed by local indentation of the tube cross sections. With low impact velocities, the tube damage resembled the shape of the indenter with small damage extension along the circumferential and longitudinal directions. As the impact energy increased, the effects of the indenter shape on the tube damage decreased, and the circumferential and longitudinal damage extension dominated and produced damage in the shape of a diamond. The corresponding numerical simulations are shown in Fig. 13 (b) and (c), and they indicate that the simulation results without strain rate and with strain rate of C=4000 and p=5 are similar in local deformation modes. When compared with experimental data, the sizes of dents in the numerical models without strain rate were similar to the test results at low impact energies (e.g., v = 0.89 m/s). However, for high impact energies (e.g., v = 2.35 m/s), the sizes of the dents in the models considering strain rate effects were more consistent with the test outcomes.

The tube cross sections (CS01, CS03 and CS05) after impacts are shown in Fig. 14. It is found that top segments of the damaged tubes from the experiments were almost flat by visual judgement. However, in reality, the shoulders at the two corners of the deformed tube cross sections were slightly higher than that at the mid-tube, which were confirmed by the observations from Fig. 14 (e) and (f). This is more visible from numerical simulations. The differences were very small, though.

The damage shapes of the tubes were quantified, as shown in Table 6, according to the parameters defined in Fig. 12. The distance between the two corners, d_1, increased noticeably with increasing impact speed. The included angle β between the crease and the diagonal in the circumferential direction slightly increased with increasing impact velocity, which caused some

measurement errors due to the difficulty of identifying the extension direction of the wide creases. Another characteristic dimension d_2, along the length of the tube, could be calculated from the geometry of the diamond-like shape of a dent. The distance d_1 in the tests was slightly larger than that in the simulation results, which was confirmed by the observations in Fig. 13. According to the comparison between the tests and FE models, the included angles and the values of d_2 were acceptable and reasonable to a certain extent.

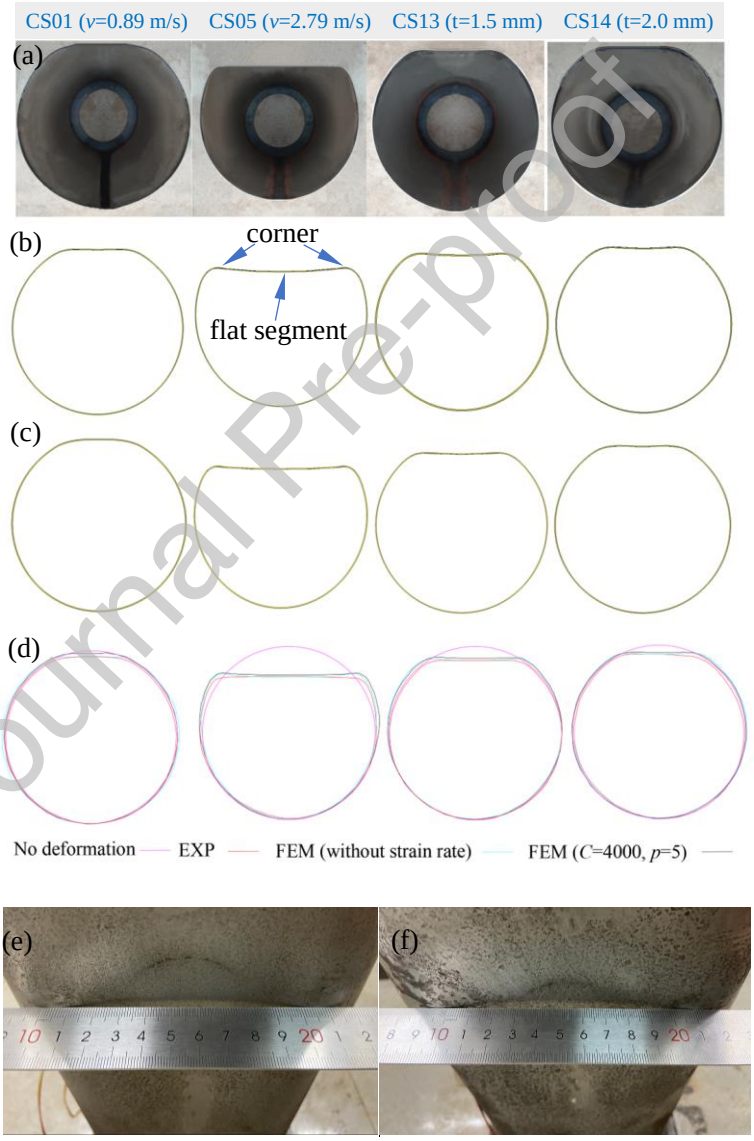

Fig. 14. (a)~(c): cross sections of the tubes from the experiments, FEM (without strain rate), and FEM (C=4000 and p=5); (d) comparison of cross sections between the experiments and numerical simulations; (e) and (f): dent depth at the mid-tube.

Table 6. Dent shape measurements of the steel tubes.

Case	EXP			FEM (without strain rate)			FEM (C =4000, p=5)		
	d_1(mm)	β (°)	d_2 (mm)	d_1(mm)	β (°)	d_2 (mm)	d_1(mm)	β (°)	d_2 (mm)
CS01	72	61	129	71	61	128	69	60	120
CS02	87	64	178	92	65	197	88	64	180
CS03	144	63	283	130	66	292	124	65	266
CS04	160	64	328	143	66	321	138	65	296
CS05	176	64	361	165	66	371	159	66	357
CS06	114	63	224	114	65	244	110	65	236
CS07	130	62	244	120	65	257	117	65	251
CS08	132	64	271	128	65	274	124	65	266
CS09	135	63	265	129	66	290	124	65	266
CS10	115	64	236	112	65	240	109	64	223
CS11	143	65	307	134	65	301	130	66	291
CS12	155	63	304	149	65	320	143	65	307
CS13	105	60	182	104	66	234	96	66	216
CS14	80	58	128	80	59	133	76	58	122

The damaged longitudinal sections of the tubes at an impact velocity of 2.79 m/s were depicted in Fig. 15 (a), (b) and (c) . These figures show that the longitudinal deflections in the numerical models extended to the tube ends even when the strain rate effects were considered. However, in the experiments, no visible deflections were observed near the tube ends. A more detailed comparison of the tube longitudinal deformations portrayed on the same graph was performed, as shown in Fig. 15 (d), including a theoretical-deflection expression developed by Wierzbicki and Suh [28]. This expression is given as $w = w_d(1 - \frac{x}{\xi})^2$, where w_d is the tube deformation at the impact point, and $\xi = \sqrt{\frac{\pi D^2 w_d}{6t}}$ is half the dented region length along the tube length. According to the theoretical

formula, 2ξ is 1.61 m larger than the total length of the tube, which is not applicable in this work. Based on the observations from the numerical results, we assumed that ξ was equal to half the tube length to perform the comparison. The results in Fig. 15 (d) show that the deflections of the experiment and numerical models (without strain rate) were in good agreement at the mid span, but displayed evident deviations at the tube ends. The theoretical formula did not produce good results at the impact point due to the size effects of the indenter, but it produced good agreement with the test at the tube ends.

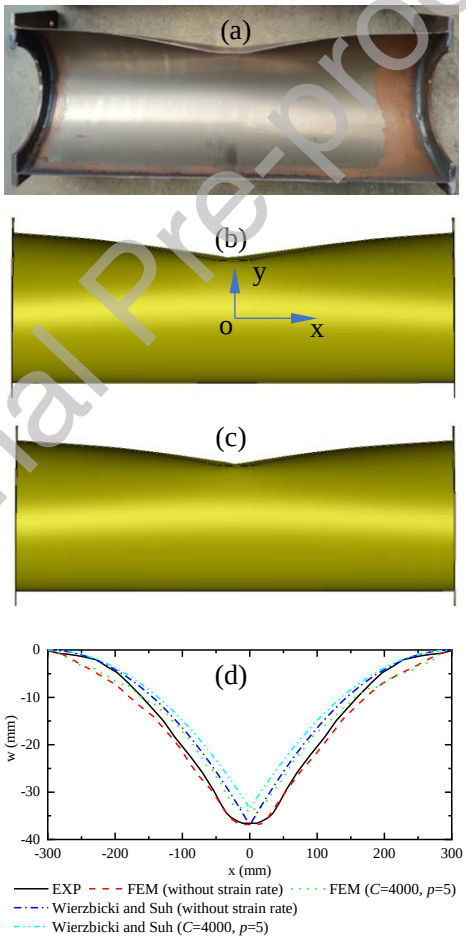

Fig. 15. Longitudinal sections of the tubes at the impact point: (a) experiment, (b) FEM (without strain rate), (c) FEM (C=4000 and p=5) and (d) comparison of longitudinal-section deformation.

5.2. Test group 2: CS03, CS06~09 with different masses

Fig. 16 shows the impact force-time history and impact force-deformation curves in CS06 and CS09, respectively. The results show that the peak forces and deformations varied slightly with increasing mass. The impact force-deformation curves for both the tests and simulations were plotted on the same graph, as shown in Fig. 17. The results show that the loading and unloading processes in the numerical models were not influenced by the mass changes, but in the tests, the slopes in the damage extension stage slightly grew with increasing mass. Hence, the strain rate effects should be considered in the FE models under such an impact velocity of 1.85 m/s, as the outcomes simulated by using the numerical models considered strain rate effects with C=4000 and p=5. Fig. 18 shows the deformation modes of the steel tubes, illustrating that the shapes of damage of the tubes resembled diamonds which increased slightly in size with increasing mass. The shapes of the dents on the tubes in the FE models with strain rate of C=4000 and p=5 were closer to the experimental results than those of the models without strain rate.

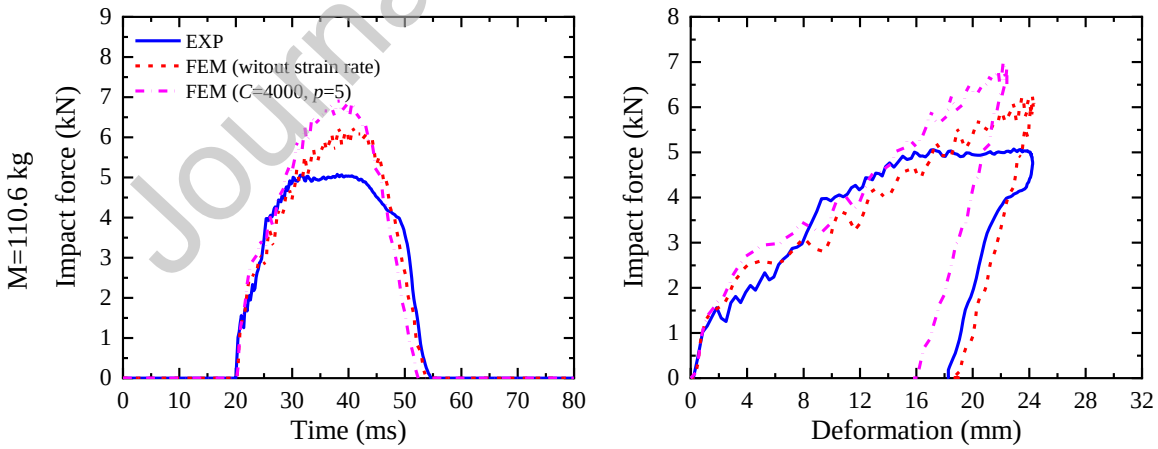

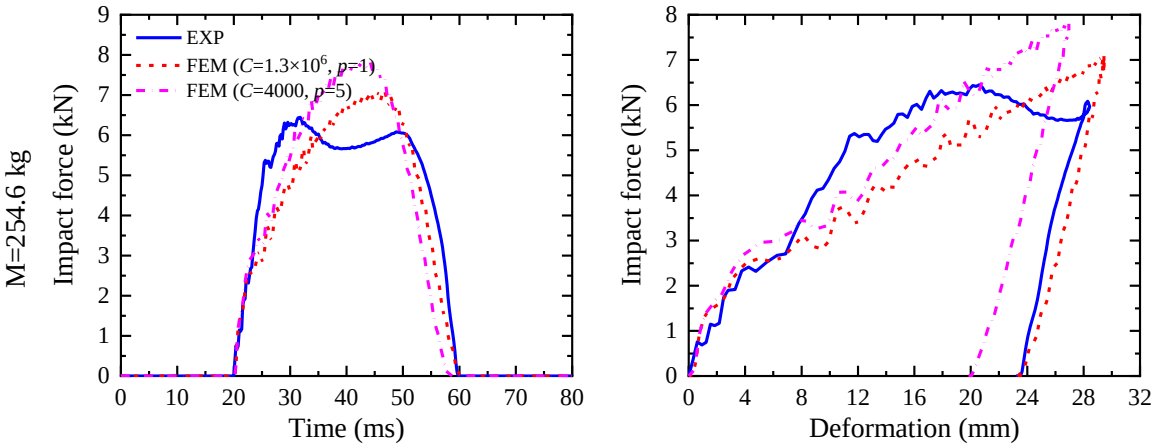

(a) Force versus time (b) Force versus deformation

Fig. 16. Impact force-time history and impact force-deformation curves with different masses.

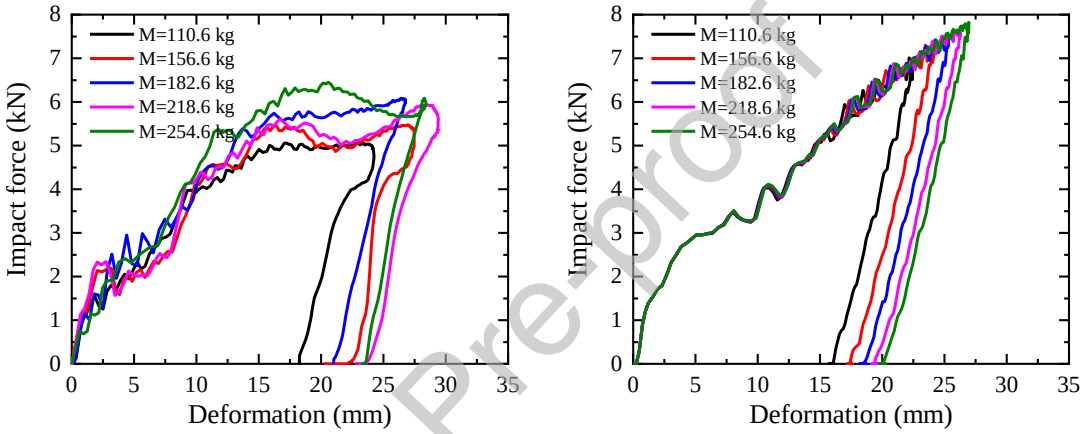

(a) Experiment (b) FEM (C=4000, p=5)

Fig. 17. Force versus deformation curves with different masses.

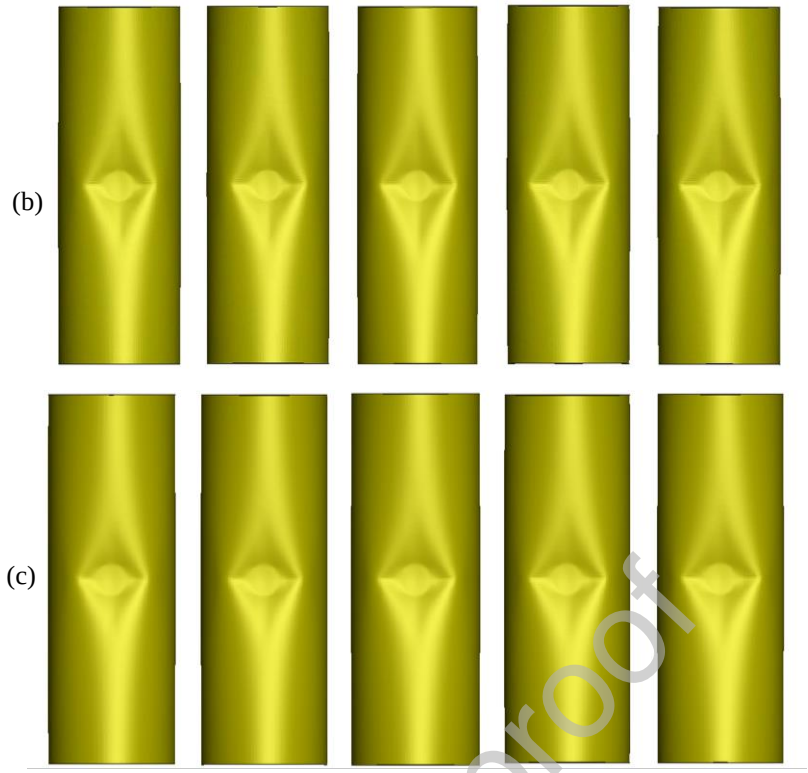

Fig. 18. Deformation modes of steel tubes with different masses: (a) experiment, (b) FEM (without strain rate) and (c) FEM (C=4000 and p=5).

5.3. Test group 3:CS03, CS10~12 with different diameters

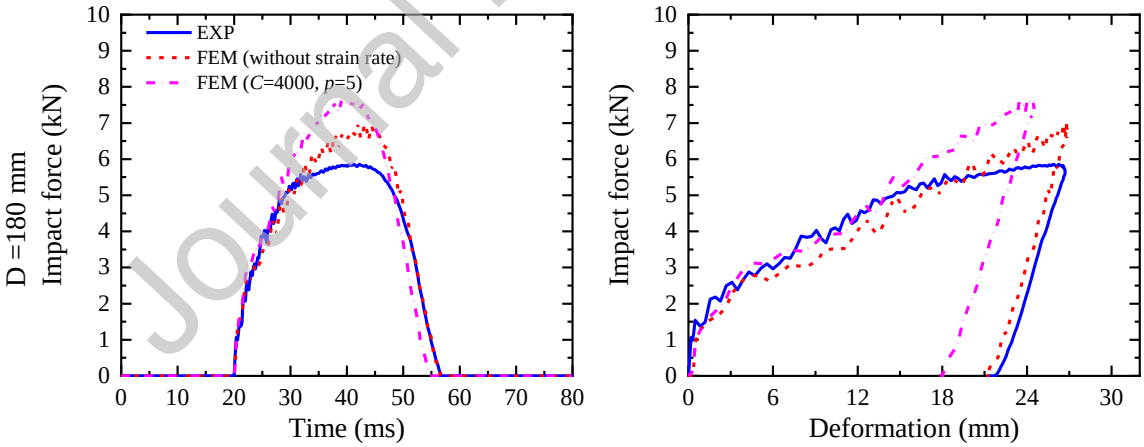

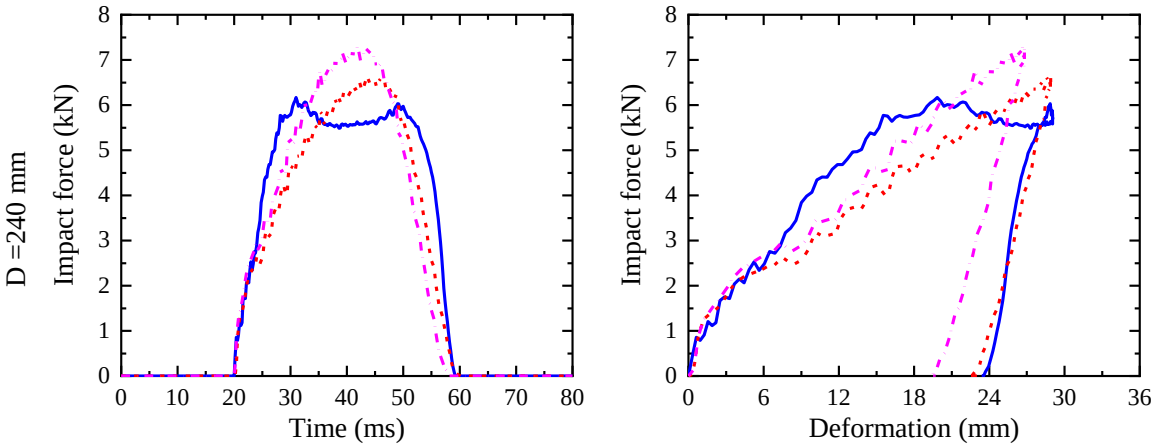

(a) Force versus time (b) Force versus deformation

Fig. 19. Impact force-time history and impact force-deformation curves with different diameters.

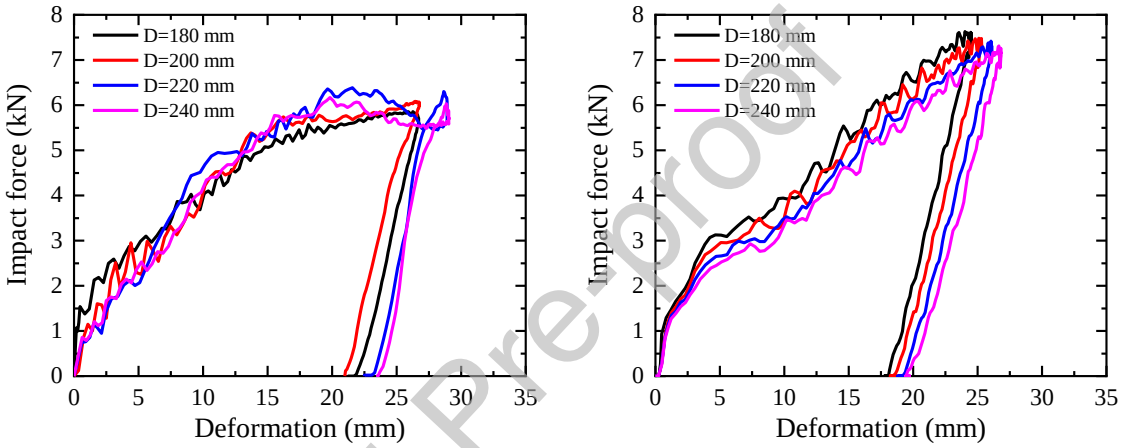

(a) Experiment (b) FEM (C=4000, p=5)

Fig. 20. Force versus deformation curves considering different diameters.

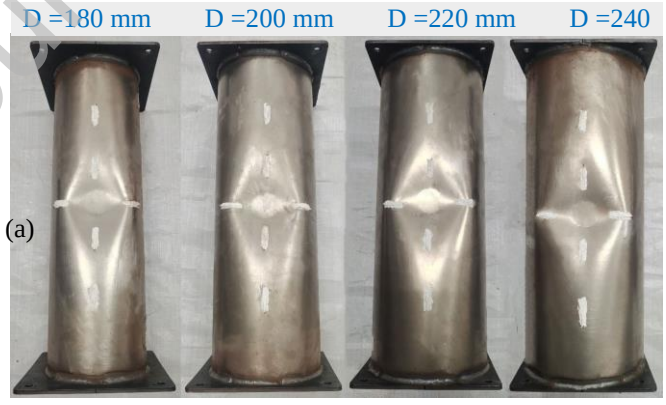

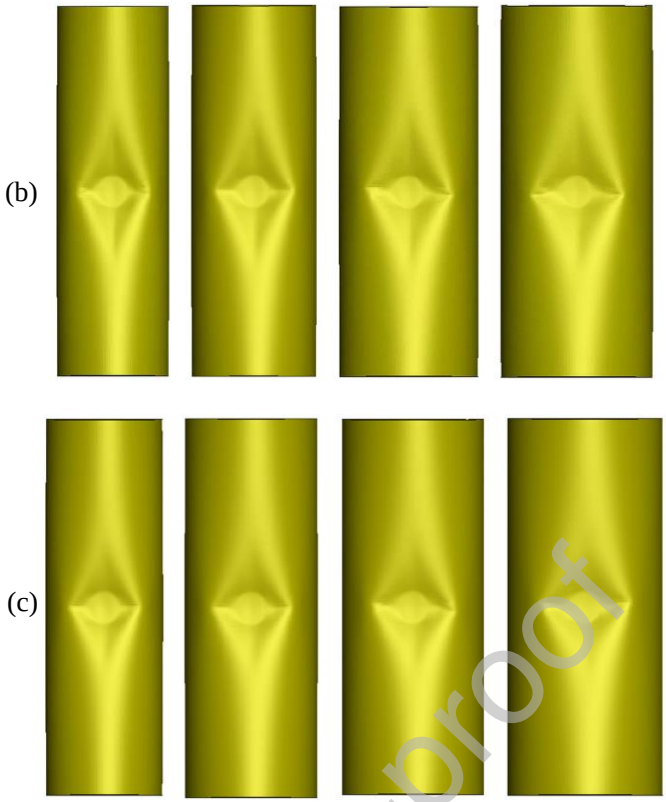

Fig. 21. Deformation modes of steel tubes with different diameters: (a) experiment, (b) FEM (without strain rate) and (c) FEM (C=4000 and p=5).

Depicted in Fig. 19 are the impact force-time record and impact force-deformation curves for diameters of 180 mm and 240 mm, respectively, which illustrate that the peak forces and deformations differed a little with increasing diameter. Fig. 20 (b) shows that the increase in the diameter decreased the local bearing capacity of the tubes. The test results in Fig. 20 (a), however, indicated that the strain rate effects became more significant with the increase of the diameter, so that the local bearing capacities of the tubes hardly decreased and even became larger. Fig. 21 shows the deformation modes of the steel tubes, indicating that the dent shapes of the tubes resembled diamonds that increased a little in size with diameter and were gradually dominated by a greater circumferential damage extension.

5.4. Test group 4: CS03, CS12~14 with different thicknesses

Fig. 22 plots the impact force-time record and impact force-deformation curves with wall

thicknesses of 1.5 mm and 2.0 mm, respectively, indicating that the variations in the thickness strongly influence the peak forces and deformations for the same impact energy and that the strain rate effects gradually became insignificant due to small deformation. The cross sections of the tubes in the tests and numerical models were in good agreement, as shown in Fig. 14. The deformation modes of the tubes with varied thicknesses are shown in Fig. 24. The results indicated that the local indentations of the tubes evolved from diamond-shaped dents governed by the circumferential and longitudinal extension to oval-shaped dents related to the indenter shape. This was because the increase in wall thickness increased the local bearing capacity of the tubes.

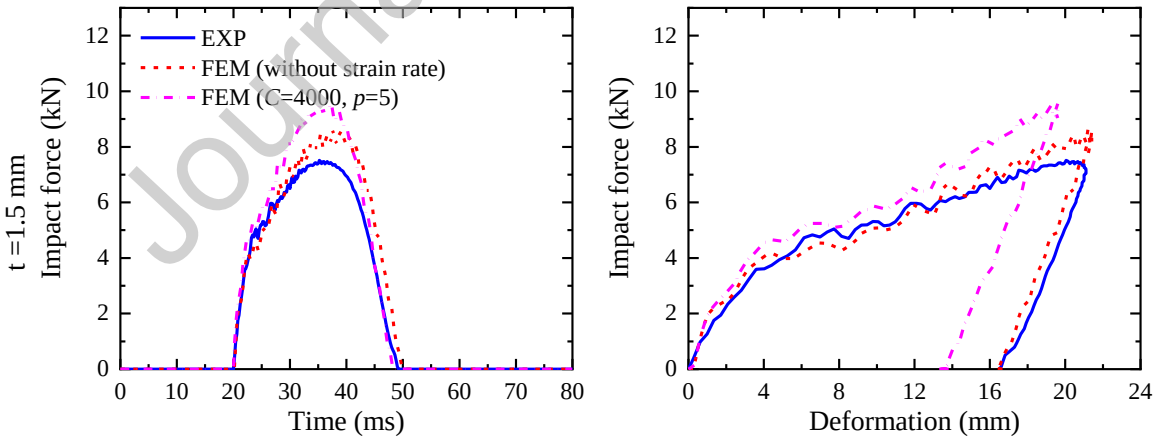

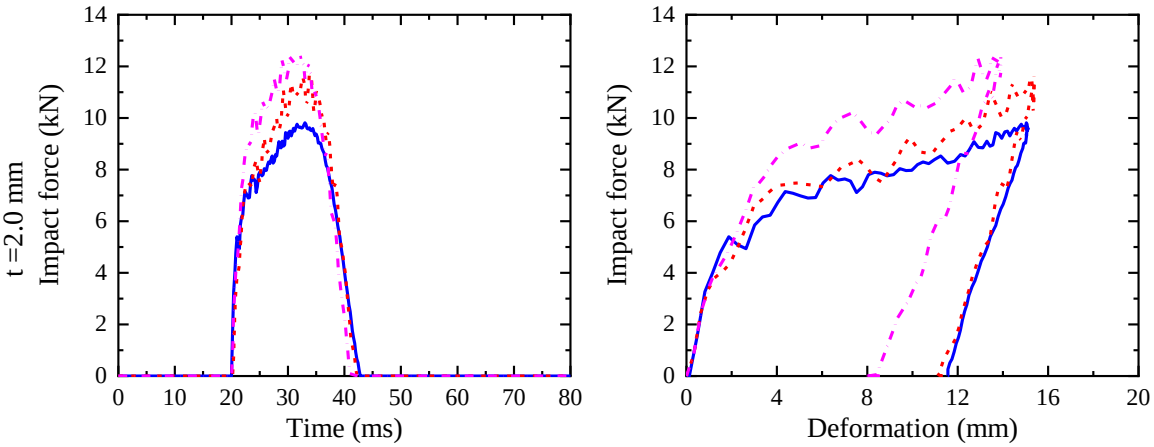

(a) Force versus time (b) Force versus deformation

Fig. 22. Impact force-time history and impact force-deformation curves with different thicknesses.

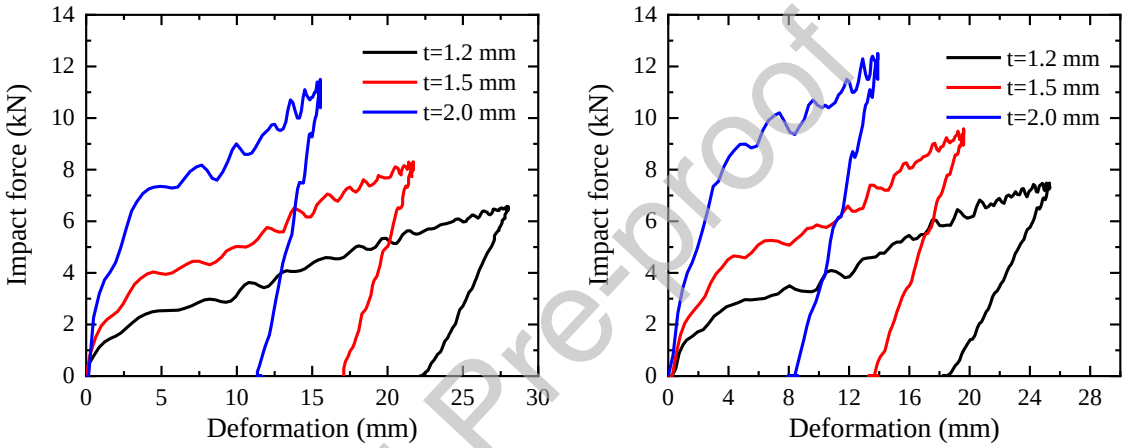

(a) Experiment (b) FEM (C=4000, p=5)

Fig. 23. Force versus deformation curves considering different diameters.

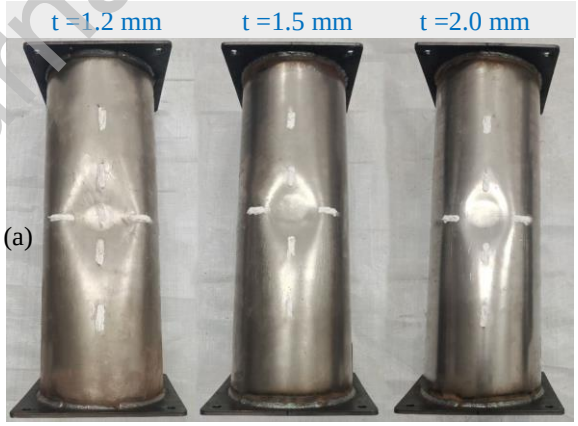

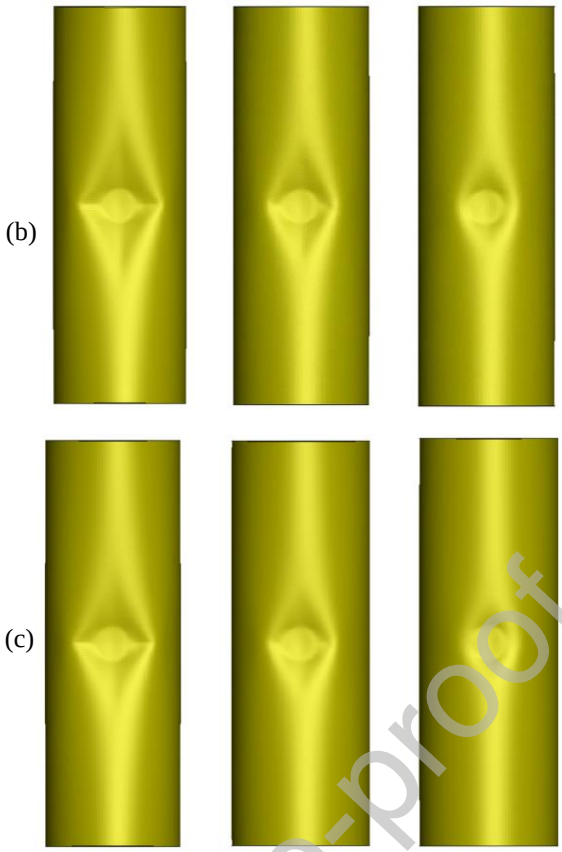

Fig. 24. Deformation modes of steel tubes with different wall thickness: (a) experiment, (b) FEM (without strain rate) and (c) FEM (C=4000 and p=5).

5.5. Impulse and energy analysis

The impulses and strain energies during the impact, which represent the area under the force-time and force-displacement curves respectively, are summarized in Table 7 and Table 8. The results show that the impulse and energy errors between the tests and the numerical models presented positive and negative variations without evident regularities. Also, the strain rate effects had no positive influences on error reduction.

Table 7. Impulse error (impulse unit: N·s).

	I_1 (EXP)	I_2 (FEM (without strain rate))	error	I_3 (FEM (C=4000 and p=5))	error
CS01	85.8	90.4	5.4%	96.4	12.4%
CS02	123.6	125.2	1.3%	131.0	6.0%
CS03	178.2	171.6	-3.7%	178.9	0.4%
CS04	225.1	213.3	-5.2%	220.1	-2.2%
CS05	289.5	251.4	-13.2%	257.9	-10.9%
CS06	133.5	141.2	5.8%	147.6	10.6%
CS07	151.5	158.3	4.5%	165.6	9.3%

CS08	174.6	180.3	3.3%	188.9	8.2%
CS09	198.4	189.4	-4.5%	197.2	-0.6%
CS10	159.7	171.4	7.3%	178.6	11.8%
CS11	191.4	171.7	-10.3%	179.0	-6.5%
CS12	186.8	172.3	-7.8%	179.4	-4.0%
CS13	154.6	174.7	13.0%	183.2	18.5%
CS14	162.6	176.7	8.7%	186.7	14.8%

Table 8. Energy error (energy unit: J).

Case	E_1 (EXP)	E_2 (FEM (without strain rate))	error	E_3 (FEM (C=4000 and p=5))	error
CS01	20.2	19.9	-1.5%	16.2	-19.8%
CS02	44.9	43.8	-2.4%	40.2	-10.5%
CS03	96.9	94.2	-2.8%	88.7	-8.5%
CS04	165.3	155.9	-5.7%	149.6	-9.5%
CS05	244.3	220.6	-9.7%	214.0	-12.4%
CS06	72.9	75.4	3.4%	70.2	-3.7%
CS07	88.2	86.2	-2.3%	80.6	-8.6%
CS08	106.6	101.5	-4.8%	95.2	-10.7%
CS09	114.3	106.0	-7.3%	100.0	-12.5%
CS10	102.5	94.9	-7.4%	89.4	-12.8%
CS11	102.0	94.4	-7.5%	88.6	-13.1%
CS12	108.7	94.1	-13.4%	88.3	-18.8%
CS13	93.8	93.1	-0.7%	86.4	-7.9%
CS14	89.9	95.9	6.7%	88.5	-1.6%

The energy dissipated in the struck tubes was calculated in the evaluation of external dynamics. The related assessment formula with respect to the strain energy dissipation of ship collision with installation in normal direction was given by Popov et al. [41] and can be written as:

$$E_s = \frac{1}{2}\overline{m}_s\bar{v}_s^2\frac{(1-\frac{\bar{v}_i}{\bar{v}_s})^2}{1+\frac{\overline{m}_s}{\overline{m}_i}} \quad (8)$$

where $\bar{v}_s$ and $\bar{v}_i$ are the velocities of the ship and installation, respectively, taken normal to the impact plane. In most cases, the velocity of installation is equal to zero. $\overline{m}_s$ and $\overline{m}_i$ are the masses of the ship and installation, respectively.

Here, we considered only the simplest case of normal impact related to the scenarios in this

paper; other detailed descriptions in Eq. (8) can be found in Refs. [2, 41]. In the present study, $\bar{v}_s$ is equal to the initial impact velocity, and $\bar{m}_s$ is the pendulum mass.

Table 9. Evaluation of strain energy dissipation (energy unit: J).

Case	E_0 (initial kinetic energy)	E_1 (EXP)	$\frac{E_1}{E_0}\times100\%$	E_2 (FEM (without strain rate))	$\frac{E_2}{E_0}\times100\%$	E_3 (FEM (C=4000 and p=5))	$\frac{E_3}{E_0}\times100\%$	E_4 (Eq. (8))	$\frac{E_4}{E_0}\times100\%$
CS01	40.0	20.2	50.5%	19.9	49.7%	16.2	40.5%	25.8	64.4%
CS02	84.0	44.9	53.5%	43.8	52.2%	40.2	47.9%	54.1	64.4%
CS03	172.8	96.9	56.1%	94.2	54.5%	88.7	51.3%	111.3	64.4%
CS04	278.9	165.3	59.3%	155.9	55.9%	149.6	53.6%	179.6	64.4%
CS05	393.1	244.3	62.2%	220.6	56.1%	214.0	54.4%	253.1	64.4%
CS06	172.8	72.9	42.2%	75.4	43.6%	70.2	40.6%	90.3	52.3%
CS07	172.8	88.2	51.0%	86.2	49.9%	80.6	46.7%	102.3	59.2%
CS08	172.8	106.6	61.7%	101.5	58.8%	95.2	55.1%	118.2	68.4%
CS09	172.8	114.3	66.1%	106.0	61.4%	100.0	57.9%	123.7	71.6%
CS10	172.8	102.5	59.3%	94.9	54.9%	89.4	51.7%	111.2	64.3%
CS11	172.8	102.0	59.0%	94.4	54.6%	88.6	51.3%	111.4	64.4%
CS12	172.8	108.7	58.8%	94.1	54.4%	88.3	51.1%	111.4	64.5%
CS13	172.8	93.8	54.2%	93.1	53.9%	86.4	50.0%	111.5	64.5%
CS14	172.8	89.9	52.1%	95.9	55.5%	88.5	51.2%	111.8	64.7%

By comparing the ratios of the dissipated energy to initial kinetic energy among the experiments, numerical simulations and analytical method, Table 9 shows that the results calculated by the analytical method were the largest, followed by the experimental results, and the numerical results were the smallest. The minimum value of the difference in the energy ratio exceeded 5% between the tests and analytical method and 8% between the numerical simulations without the strain rate and analytical method. Additionally, the consideration in the strain rate effects further decreased the energy dissipation ratio. Therefore, the results calculated by Eq. (8) may be conservative for practical engineering design.

5.6. Comparison with two quasi-static solutions for indentation of tubes

Theoretical models are useful tools for quick and reliable assessments of structural responses under accidental loads and are also widely used in design rules and standards (e.g., DNV RP C204

[33]). A few analytical models are available in the literature for the indentation resistance of tubes subjected to lateral loading. These models, however, are generally designed for long slender tubes, e.g., jacket braces and legs, with large-area contact loading. Their applicability to large diameter tubes under concentrated impacts remains to be examined.

Amdahl [26] proposed a local denting model based on a plastic yield line analysis, and the model related the denting resistance to local indentation. This model used a flat indenter and considered the contact width effect. The cross section with a flat segment at the side of the contact surface is similar to the results of the present study. The model is adopted in NORSOK N-004 [27], and the form of the denting resistance is as follows:

$$\frac{R}{R_c} = \left(22 + 1.2\frac{B}{D}\right)\left(\frac{w_d}{D}\right)^{\frac{1.925}{3.5+\frac{B}{D}}}\sqrt{\frac{4}{3}\left[1-\frac{1}{4}\left(1-\frac{N}{N_P}\right)^3\right]} \tag{9}$$

where B is the contact width of the indenter, D is the tube diameter, w_d is the dent depth, N is the axial load, and N_P is the plastic yield resistance. The last term was borrowed from Wierzbicki and Suh [28] to account for the effect of axial functional loads in the leg. R_c is a characteristic resistance of the tube and is defined as:

$$R_c = \sigma_y \frac{t^2}{4}\sqrt{\frac{D}{t}} \tag{10}$$

Wierzbicki and Suh [28] derived a closed form solution for the indentation resistance of tubes under combined loading in the form of lateral indentation, bending moment and axial force. The problem was decoupled into the bending and stretching of a series of unconnected rings and generators. The indentation resistance is given as:

$$R = 16\sqrt{\frac{2\pi}{3}\frac{D}{t}\frac{w_d}{D}\frac{1}{4}}\sigma_y 4t^2\sqrt{\left[1-\frac{1}{4}\left(1-\frac{N}{N_P}\right)^3\right]} \tag{11}$$

Fig. 25 compares indentation resistances from experiments, numerical simulations and theoretical models. It is found that the theoretical models predict much larger resistance (almost doubled) than the experimental and numerical results, which is very unconservative. The reason may be that the analytical models assume large contact loading rather than concentrated in the experiments, which leads to different cross section deformation patterns and resistances.

In order to further illustrate the relationship between the resistances and indentations, Fig. 26 and Fig. 27 display the nondimensionalized force-deformation curves for all cases in both experiments and numerical simulations with respect to R_c. The curves from the numerical simulations tend to merge into a single curve after being nondimensionalized. The nondimensional experimental curves are however more scattered but with the same trend. The nondimensional curves for cases of CS10~14 with different diameter to thickness ratios deviate slightly from the merged curve at the initial collapse stage and a smaller D/t leads to increased capacities. In the absence of new analytical formulations for large diameter tubes subjected to concentrated loading, a piecewise fitted curve is recommended in Fig. 27 for structural design based on curve fitting of the nondimensional force-deformation curves from numerical simulations. The formulation for the piecewise fitted curve is given as:

$$\frac{R}{R_c} = \begin{cases} 8.5\left(\frac{w_d}{D}\right)^{0.45}, & 0 < \frac{w_d}{D} < 0.04 \\ 30.2\frac{w_d}{D} + 0.8, & 0.04 \le \frac{w_d}{D} \end{cases} \qquad (12)$$

The fitted formulation can be conservative for tubes with small D/t.

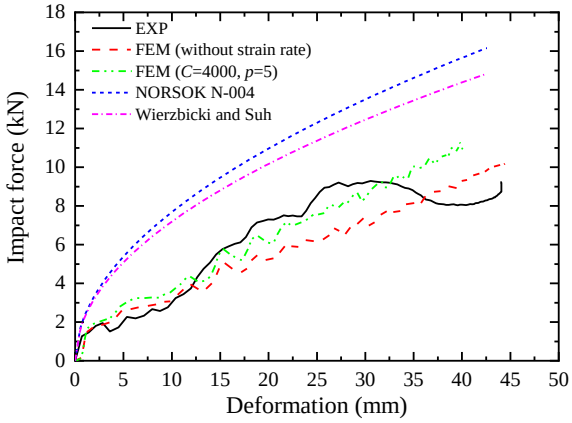

Fig. 25. Comparison of indentation resistances.

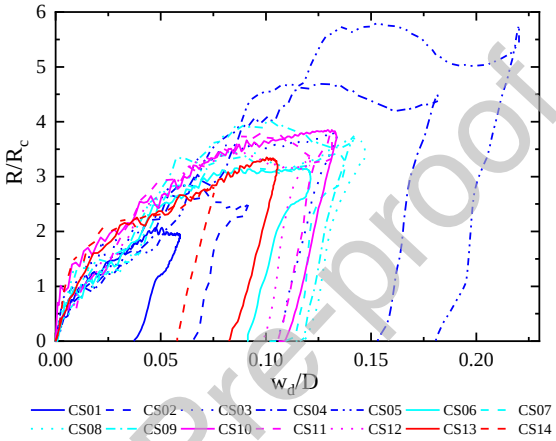

Fig. 26. Dimensionless force-deformation curves of the experiments.

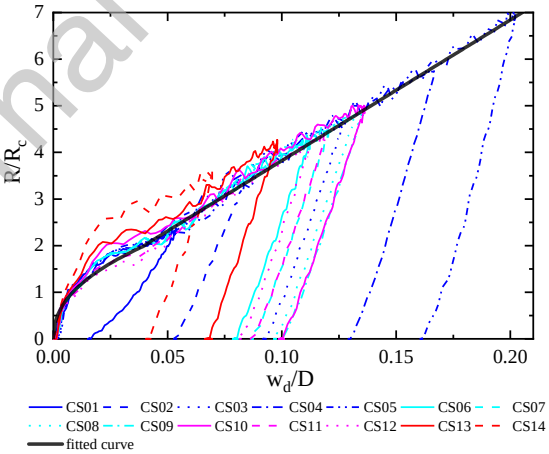

Fig. 27. Dimensionless force-deformation curves from the numerical simulations (C=4000, p=5).

5.7. Discussions

The impact resistance and damage of large diameter steel tubes under concentrated lateral impact loads were investigated by the experimental tests at a scaling factor of 1:30 and numerical simulations. Scaled model tests can generally reproduce responses of a geometrically similar

full-scale model. However, scaling effects exist, which may cause differences with full scale test results, Notably the strain rate effect. Structures subjected to dynamic loads do not follow the usual similarity laws when the material strain rate effect becomes important as discussed in refs[42-44]. In this study, the impact velocity is low, which leads to a small strain rate. Therefore, the difference of the responses of the tubes between the scaled model and protype is not very remarkable. Many scaled model test results [45] also confirm limited influence of the strain rate effect in low velocity impacts.

6. Conclusions

This paper studies the deformation behaviors of large diameter steel tubes from a FOWT under concentrated lateral impact loads using experiments and numerical simulations. Fourteen test tubes were designed and fabricated with a scale of 1:30. These tubes were divided into 4 groups with respect to impact velocities, attached masses, diameters, and thicknesses. Nonlinear FE simulation using LS-DYNA were conducted to reproduce the test in cases with and without considering the strain rate effects. The results were compared and discussed. The following conclusions were drawn:

(1) Deformation of large diameter tubes could generally be divided in three phases: (Ⅰ) initial collapse, with small local dent resembling the shape of the indenter. (Ⅱ) damage extension stage, with plastic deformation extending progressively in longitudinal and circumferential directions. (Ⅲ) elastic unloading with deformation recovery.

(2) The deformation modes of large diameter tubes were governed by the local indentations of tube cross sections with flat segments at topside. The dented shapes progressively developed to

resemble a diamond with increasing impact energy.

(3) Numerical simulations with strain rate effects reasonably reproduced the force-deformation curves from experiments. By neglecting strain rate effects, the simulation results became conservative.

(4) Existing models for indentation of slender tubes did not apply to large diameter tubes, and significantly overestimated the experimental force-deformation curves. This was because the deformation modes of cross sections differed. Deformation of the slender tubes extended over the whole cross section while for large diameter tubes, the cross section deformed only partly. This indicated needs for new analytical models for large diameter tubes. In the absence of a more appropriate model, a nondimensional force-deformation curve based on the numerical simulations was recommended for design purposes.

Author Contributions

Yongli Ren: Conceptualization, Methodology, Investigation, Test, Software, Writing - original draft, Writing - review & editing. Zhaolong Yu: Methodology, Investigation, Software, Supervision, Writing - review & editing. Xugang Hua: Conceptualization, Investigation, Supervision, Writing - review & editing. Jørgen Amdahl: Methodology, Investigation, Supervision, Writing - review & editing. Zili Zhang: Conceptualization, Investigation, Supervision. Zhengqing Chen: Supervision.

Declaration of Competing Interest

The authors declare no conflict of interest.

Acknowledgments

The first author gratefully acknowledges financial support from the Chinese Scholarship Council

under the State Scholarship Fund. The support of the Intergovernmental International Innovation Cooperation of China National Key Research and Development Plan (Grant Number: 2016YFE0127900) is also greatly acknowledged. The second and fourth authors would like to acknowledge financial support by Research Council of Norway via the Centers of Excellence funding scheme, project number 223254 – NTNU AMOS.

References

[1] DNV G L. DNV GL-ST-0119 Floating wind turbine structures. DNV GL, Høvik, Norway, 2018.

[2] Yu Z, Amdahl J, Rypestøl M, Cheng Z. Numerical modelling and dynamic response analysis of a 10 MW semi-submersible floating offshore wind turbine subjected to ship collision loads. Renew. Energy 2022; 184: 677-699.

[3] Moulas D, Shafiee M, Mehmanparast A. Damage analysis of ship collisions with offshore wind turbine foundations. Ocean Eng 2017; 143: 149-162.

[4] Bela A, Le Sourne H, Buldgen L, Rigo P. Ship collision analysis on offshore wind turbine monopile foundations. Mar Struct 2017; 51: 220-241.

[5] Song M, Jiang Z, Yuan W. Numerical and analytical analysis of a monopile-supported offshore wind turbine under ship impacts. Renew Energy 2021; 167: 457-472.

[6] Lee K. Effects on the various rubber fenders of a tripod offshore wind turbine substructure collision strength due to boat. Ocean Eng 2013; 72: 188-194.

[7] Echeverry S, Marquez L, Rigo P, Le Sourne H. Numerical crashworthiness analysis of a spar floating offshore wind turbine impacted by a ship. Proceedings of the 8th international conference on collision and grounding of ships and offshore structures (ICCGS 2019), October 2019. Lisbon, Portugal: CRC Press.

[8] Ren Y, Meng Q, Chen C, Hua X, Zhang Z, Chen Z. Dynamic behavior and damage analysis of a spar-type

floating offshore wind turbine under ship collision. Eng Struct 2022; 272: 114815.

[9] Jonkman, J. Definition of the Floating System for Phase IV of OC3. National Renewable Energy Laboratory, Golden, Colorado, 2010.

[10] Jonkman J, Butterfield S, Musial W, Scott G. Definition of a 5-MW reference wind turbine for offshore system development. National Renewable Energy Lab. (NREL), Golden, CO (United States), 2009.

[11] Le Sourne H, Donner R, Besnier F, Ferry M. External dynamics of ship-submarine collision. In: 2nd International Conference on Collision and Grounding of Ships; 2001.

[12] Zhang Y, Hu Z, Ng C, Jia C, Jiang Z. Dynamic responses analysis of a 5 MW spar-type floating wind turbine under accidental ship-impact scenario. Mar Struct 2021; 75: 102885.

[13] Zhang Y, Hu Z. An aero-hydro coupled method for investigating ship collision against a floating offshore wind turbine. Mar Struct 2022; 83: 103177.

[14] Ladeira I, Márquez L, Echeverry S, Le Sourne H, Rigo P. Review of methods to assess the structural response of offshore wind turbines subjected to ship impacts. Ships Offshore Struct 2022; 1-20.

[15] Thomas SG, Reid SR, Johnson W. Large deformations of thin-walled circular tubes under transverse loading—I: an experimental survey of the bending of simply supported tubes under a central load. Int J Mech Sci 1976; 18(6): 325-333.

[16] Watson AR, Reid SR, Johnson W, Thomas SG. Large deformations of thin-walled circular tubes under transverse loading—II: Experimental study of the crushing of circular tubes by centrally applied opposed wedge-shaped indenters. Int J Mech Sci 1976; 18(7-8): 387-397.

[17] Watson AR, Reid SR, Johnson W. Large deformations of thin-walled circular tubes under transverse loading—III: further experiments on the bending of simply supported tubes. Int J Mech Sci 1976; 18(9-10): 501-502.

[18] Soares CG, Søreide TH. Plastic analysis of laterally loaded circular tubes. J Struct Eng 1983; 109(2): 451-467.

[19] Jones N. Quasi-static analysis of structural impact damage. J Constr Steel Res 1995; 33(3): 151-177.

[20] Ong LS, Lu G. Collapse of tubular beams loaded by a wedge-shaped indenter. Exp. Mech 1996; 36(4): 374-378.

[21] Jones N, Shen WQ. A theoretical study of the lateral impact of fully clamped pipelines. Proc Inst Mech Eng Part E-J Process Mech Eng 1992; 206(2): 129-146.

[22] Zhu L, Liu Q, Jones N, Chen M. Experimental study on the deformation of fully clamped pipes under lateral impact. Int J Impact Eng 2018; 111: 94-105.

[23] Zhang R, Zhi X, Fan F. Plastic behavior of circular steel tubes subjected to low-velocity transverse impact. Int J Impact Eng 2018; 114: 1-19.

[24] Zhi X, Zhang R, Fan F, Huang C. Experimental study on axially preloaded circular steel tubes subjected to low-velocity transverse impact. Thin-Walled Struct 2018; 130: 161-175.

[25] Søreide TH, Amdahl J. Deformation characteristics of tubular members with reference to impact loads from collision and dropped objects. Norwegian Maritime Research Paper 2, Norwegian Maritime, 1982; 3-12.

[26] Amdahl J. Impact Capacity of Steel Platforms and Tests on Large Deformations of Tubes and Transverse Loading. Det norske Veritas. Progress Report (10), 1980, 80–0036.

[27] NORSOK, 2004. NORSOK Standard N004. Design of Steel Structures, Appendix a, Design against Accidental Actions. Det Norske Veritas, 2004.

[28] Wierzbicki T, Suh MS. Indentation of tubes under combined loading. Int J Mech Sci 1988; 30(3-4): 229-248.

[29] Yu Z, Amdahl J. A review of structural responses and design of offshore tubular structures subjected to ship impacts. Ocean Eng 2018; 154: 177-203.

[30] Zhang Z, Høeg C. Inerter-enhanced tuned mass damper for vibration damping of floating offshore wind turbines. Ocean Eng 2021; 223: 108663.

[31] Meng Q, Hua X, Chen C, Zhou S, Liu F, Chen Z. Analytical study on the aerodynamic and hydrodynamic damping of the platform in an operating spar-type floating offshore wind turbine. Renew Energy 2022; 198: 772-788.

[32] Browning J R, Jonkman J, Robertson A, et al. Calibration and validation of a spar-type floating offshore wind turbine model using the FAST dynamic simulation tool. Journal of physics: conference series. IOP Publishing, 2014; 555(1): 012015.

[33] DNV-PR-C204. Recommended practice DNV-PR-C204. Det Norske Vertas 2010.

[34] Standardization Administration of China, GB/T 228.1-2010, Metallic Materials-Tensile Testing-Part 1: Method of Test At Room Temperature, Standards Press of China, 2010.

[35] LSTC, LS-DYNA keyword user's manual, Livermore Software Technology Corporation, 2018.

[36] Alsos HS, Amdahl J. On the resistance of tanker bottom structures during stranding. Mar Struct 2007; 20(4): 218-237.

[37] Ray WC, Joseph P, Wang GY. Dynamics of Structures. Berkeley, CA: Computers & Structures 1995.

[38] Villavicencio R, Soares CG. Numerical plastic response and failure of a pre-notched transversely impacted beam. Ships Offshore Struct 2012; 7(4): 417-429.

[39] Cowper J, Symonds P. Strain-hardening and strain-rate effects in the impact loading of cantilever beams. Providence(RI): Division of Applied Mathematics, Brown University. Technical Report No.: 28, 1957. Contract Nonr-562(10), NR-064-406.

[40] Storheim M, Amdahl J. On the sensitivity to work hardening and strain-rate effects in nonlinear FEM analysis of ship collisions. Ships Offshore Struct 2017; 12(1): 100-115.

[41] Popov YN, Faddeev OV, Kheisin DE, Yakovlev AA. *Strength of ships sailing in ice*. Army Foreign Science and Technology Center Charlottesville Va, 1969.

[42] Jones N. Structural impact. Cambridge University Press, Cambridge 1989.

[43] Oshiro R E, Alves M. Scaling of structures subject to impact loads when using a power law constitutive equation. Int J Solids and Struct 2009, 46(18-19): 3412-3421.

[44] Oshiro R E, Alves M. Scaling of cylindrical shells under axial impact. Int J Impact Eng 2007, 34(1): 89-103.

[45] Wen H M, Jones N. Experimental investigation of the scaling laws for metal plates struck by large masses. Int J Impact Eng 1993, 13(3): 485-505.